1 **Performance of AIRS ozone retrieval over the central Himalayas: Case studies of biomass**

2 **burning, downward ozone transport and radiative forcing using long-term observations**

3

4

5 Prajjwal Rawat[1,5], Manish Naja[1], Evan Fishbein[2], Pradeep K. Thapliyal[3], Rajesh Kumar[4], Piyush

6 Bhardwaj[4], Aditya Jaiswal[1], Sugriva N. Tiwari[5], Sethuraman Venkataramani[6], Shyam Lal[6]

7

8

9

10 [1] Aryabhatta Research Institute of Observational Sciences (ARIES), Nainital, 263001, India

11 [2] NASA Jet Propulsion Laboratory, Pasadena, CA 91109, USA

12 [3] Space Applications Centre, ISRO, Ahmedabad 380015, India

13 [4] National Center for Atmospheric Research (NCAR) Boulder, CO 80307, USA

14 [5] DDU Gorakhpur University, Gorakhpur 273009, India

15 [6] Physical Research Laboratory (PRL), Ahmedabad, 380009, India

16

17

18

19

20 **Corresponding author:** Manish Naja (manish@aries.res.in)

21

22

23

24

25

26 **Short Summary:**

27 Satellite based ozone observations have gained wide importance due to their global coverage.

28 However, satellite retrieved products are indirect and needs to be validated, particularly over

29 mountains. Here, ozonesondes launched from a Himalayan site are utilized to assess the AIRS

30 ozone retrieval. AIRS is shown to overestimate ozone in the upper troposphere and lower

31 stratosphere, while the differences with ozonesonde are lower in the middle troposphere and

32 middle stratosphere.

33

34

35

36

37

38

39

40

41

42

43

44

45

46

47

48

49

50

Abstract

Data from 242 ozonesondes launched from ARIES Nainital (29.40º N, 79.50º E, and 1793 m elevation) are used to evaluate the Atmospheric Infrared Sounder (AIRS) version 6 ozone profiles and total column ozone during the period 2011-2017 over the central Himalaya. The AIRS ozone products are analyzed in terms of retrieval sensitivity, retrieval biases/errors, and ability to retrieve the natural variability of columnar ozone, which has not been done so far from the Himalayan region having complex topography. For a direct comparison, averaging kernels information is used to account for the sensitivity difference between the AIRS and ozonesonde data. We show that AIRS has lower difference with ozonesonde in the lower and middle troposphere and stratosphere with nominal underestimations of less than 20%. However, in the upper troposphere and lower stratosphere (UTLS), we observe a considerable overestimation of the magnitude as high as 102%. The weighted statistical error analysis of AIRS ozone shows higher positive bias and standard deviation in the upper troposphere of about 65% and 25%, respectively. Similar to AIRS, Infrared Atmospheric Sounding Interferometer (IASI) and Cross-track Infrared Sounder (CrIS) are also able to produce ozone peaks altitude and gradients successfully. However, the statistical errors are again higher in the UTLS region that are likely related to larger variability of ozone, lower ozone partial pressure and inadequate retrieval information on the surface parameters. Furthermore, AIRS fails to capture the monthly variation of the total ozone column, with a strong bimodal variation, unlike unimodal variation seen in ozonesonde and Ozone Monitoring Instrument (OMI). In contrast, the UTLS and tropospheric ozone column are in reasonable agreement. Increases in ozone of 5 - 20% (in 2 - 6 km altitude) after the biomass burning and during events of downward transport (in 2 - 16 km altitude) are captured well by AIRS. Ozone radiative forcing (RF) derived from total column ozone using ozonesondes data (4.86 mW/m^2) matches well with OMI (4.04 mW/m^2), while significant RF underestimation is seen in AIRS (2.96 mW/m^2). The fragile and complex landscapes of the Himalayas are more sensitive to global climate change, and establishing such biases and error analysis of space-borne sensors will help study the long-term trends and estimate accurate radiative budgets.

1. Introduction

Atmospheric ozone is an essential trace gas that plays a crucial role in the atmospheric oxidizing chemistry, air quality, and earth's radiative budget. The stratospheric ozone absorbs harmful solar ultraviolet radiation and protects biological life on earth, whereas tropospheric ozone, being a secondary air pollutant (Logan et al., 1985; Pitts and Pitts, 1997; Pierce et al., 2009) and greenhouse gas, contributes to global warming and can harm human health and crops when present in higher concentrations near the surface (Fishman et al., 1979; Ebi and McGregor 2008; Lal et al., 2017). Different radiative forcing of ozone from the stratosphere (cooling) to the troposphere (heating) (Lacis et al., 1990; Forster et al., 2007; Wang et al., 1993; Hegglin et al., 2015) demonstrate its potential importance as an atmospheric climate gas (Shindell et al., 2012). Hence, information regarding precise long-term variability in global ozone distribution is vital for better characterizing atmospheric chemistry and global climate changes (McPeters et al., 1994; Kim et al., 1996).

In recent decades, observations of ozone from space-borne sensors (microwave limb sounding, UV-VIS, and IR) have become an increasingly robust tool for global and higher temporal monitoring (Fishman et al., 1986; Munro et al., 1998; Bhartia et al., 1996; Foret et al., 2014). This increases our ability to analyze various influences of human activities on the atmospheric chemical composition including ozone, study their long-term impact on climate (Fishman et al., 1987), and estimate reliable radiative budgets (Hauglustaine and Brasseur 2001; Gauss et al., 2003; Aghedo et al., 2011). However, the space-based sensors are indirect and measure the atmospheric composition based upon specific algorithms utilizing radiative transfer models and a-priori

104 information. Hence, the retrieval outputs need to be evaluated with certain reference instruments

105 for establishing the credibility and better utilization of space-borne data.

106 The Himalayas, a complex terrain region, has the largest abundance of ice sheets outside polar

107 regions that impacts global/regional radiative budgets and climate pervasively (e.g., Lawrence and

108 Lelieveld, 2010; Lelieveld et al., 2018). Here, the in-situ ground-based observations are very

109 sparse and limited, and complex topography along with inadequate information on the surface

110 parameters make it difficult to retrieve atmospheric composition from space-borne instruments.

111 This is because ozone weighting function, a measure of the retrieval sensitivity and a fundamental

112 retrieval component, depends upon various atmospheric parameters like surface temperature,

113 surface emissivity, and terrain height (Rodgers et al., 1976, 1990; Bai et al., 2014), which is not

114 uniform over the foot-print size of the AIRS (~ 13 km x 13 km) over the Himalayas. Usually, the

115 ozone weighting function has a shorter integrating path over the elevated terrain regions, which

116 follows a smaller weighting function and provides lesser sensitivity and higher errors in the final

117 retrievals (Coheur et al., 2005; Bai et al., 2014). Apart from the terrain height, retrieval also

118 depends on other factors like surface emissivity, atmospheric input constituents, input error

119 minimizing parameters, etc., whose accuracy matters, alters the retrieval processes abruptly, and

120 introduces error in the final retrieval.

121

122 The Atmospheric Infrared Sounder (AIRS) onboard the Aqua satellite has been providing reliable

123 vertical profiles of ozone, temperature, water vapor, and other trace gases globally twice a day

124 since 2002. Numerous validation studies of AIRS retrieved ozone have been carried out for

125 different versions since it started operating (2002). For example, Bian et al. (2007) studied AIRS

126 version 4 over Beijing and discussed the potential agreements (within 10%) between AIRS and

127   ozonesonde (GPSO3) ozone, particularly in the upper troposphere and lower stratosphere (UTLS)

128   region with the capability of AIRS to identify various Stratosphere-Troposphere Exchange (STE)

129   and transient convective events. Similarly, a study over Boulder and Lauder by Monahan et al.

130   (2007) using a similar AIRS version showed despite the larger biases in the lower and middle

131   tropospheric region, the retrieval algorithm captures the ozone variability very effectively with a

132   positive correlation of more than 70%. However, that study suggested a need for tropopause-

133   adjusted coordinates in the a-priori profiles. Both these studies (Bian et al., 2007; Monahan et al.,

134   2007) show larger biases of AIRS ozone in the lower and middle tropospheric regions, however,

135   shifts in retrieval biases and errors were seen towards the UTLS region in version 5 (Divakarla et

136   al., 2008), apart from significant improvements in the lower troposphere. The retrieval

137   methodology has also changed significantly between V4 and V5. Version 4 or earlier used

138   regression retrieval as the first guess in physical retrieval while later versions used a climatology-

139   based first guess for the physical retrieval (McPeters et al., 2007). Also, radiative transfer models,

140   selected channel sets, and clarified quality indicators have been modified and improved in all

141   successive versions.

142

143   The AIRS ozone retrieval in V5 has improved significantly with retrieval biases and root mean

144   square error (RMSE) less than 5% and 20%, respectively (Divakarla et al., 2008), over the tropical

145   regions. However, there is not much discussion and studies of the assessment for AIRS ozone over

146   the Himalayas' complex terrain, where retrieval is expected to be erroneous due to large surface

147   variability within its footprint. Also, most of the previous studies (Bian et al., 2007; Divakarla et

148   al. 2008; Pittman et al., 2009) did not utilize the averaging kernels information of the AIRS that is

149   vital for satellite evaluation.

150

151   Here, evaluation of AIRS version 6, which entirely depends upon the infra-red (IR) observations

152   after the failure of the AMSU sensor, is presented in terms of statistical analysis and ability to

153   retrieve the natural variability of ozone at various altitudes over the central Himalayan region using

154   in-situ ozonesonde observations convolved with AIRS averaging kernels. Additionally, the present

155   study assessed the AIRS retrieval algorithm using IASI and CrIS radiance information for one

156   year. AIRS columnar ozone (i.e., total, UTLS, and tropospheric columns) is also assessed with

157   ozonesonde, OMI, and Microwave Limb Sounder (MLS) observations. AIRS has a long-term data

158   set for ozone and meteorological parameters, establishing such biases and error analysis is essential

159   to make meaningful use of its data to characterize the Himalayan atmosphere, study the trends,

160   radiative budgets, perform the model evaluation and data assimilation over this region.

161

162   **2 Data and Methodology**

163   **2.1 Data Description**

164   **2.1.1 AIRS**

165   Atmospheric Infrared Sounder (AIRS) onboard Aqua satellite, in a sunsynchronous polar orbit at

166   705 km altitude, is a hyperspectral thermal infrared grating spectrometer with equatorial crossings

167   at ~13:30 local time (LT). It is a nadir scanning sensor that was deployed in orbit on May 4, 2002.

168   AIRS along with its partner microwave instrument, the Advanced Microwave Sounding Unit

169   (AMSU-A), represents the most advanced atmospheric sounding system placed in space using

170   cutting-edge infrared and microwave technologies. These instruments together observe the global

171   energy cycles, water cycles, climate variations, and greenhouse gases, however after AMSU

172   failure the retrieval now mostly depends upon the AIRS IR observations. The AIRS infrared

173   spectrometer acquires 2378 spectral samples at resolutions ($\lambda/\Delta\lambda$) ranging from 1086 to 1570 cm[-]

174   [1], in three bands: 3.74 µm to 4.61 µm, 6.20 µm to 8.22 µm, and 8.8 µm to 15.4 µm (Fishbein et

175   al., 2003; Pagano et al., 2003). The independent channels of AIRS permit retrieval of various

176   atmospheric states and constituents depending upon their corresponding spectral response even in

177   the presence of 90% cloud fraction (Susskind et al., 2003; Maddy and Barnet 2008). In this study,

178   we have used Level 2 Support physical products of AIRS (AIRS2SUP). The AIRS2SUP files

179   (~240 granules/day) possess extra information over the standard AIRS files, e.g., information on

180   averaging kernel and degree of freedom, including vertical profiles at 100 pressure levels, against

181   just 28 in the standard product.

182

183   The support product profiles contain 100 levels between 1100 and 0.016 mbar. While it has a

184   higher vertical resolution, the vertical information content is no greater than the standard product.

185   The information on averaging kernels and degree of freedoms (DOFs) is utilized to understand the

186   retrieved products more comprehensively. The DOFs of ozone, a measure of significant eigen

187   functions used in the AIRS retrieval, has an average value of 1.36 over the tropical latitude band

188   (Maddy and Barnet 2008) (Table S1), while over the balloon collocated region an average DOFs

189   of 1.62 is observed (Figure S1). In the present study, the AIRS data is flagged as best quality when

190   cloud fraction is less than 80% and degrees of freedom (DOF) is greater than 0.04. However,

191   analysis of cloud fraction over our collocated position shows (Figure S2) only 7% of observations

192   during 2011 - 2017 has a cloud fraction more than 80%.

193

194

195

2.1.2 IASI (NOAA/CLASS)

The Infrared Atmospheric Sounding Interferometer (IASI) onboard MetOp satellites with a primary focus on meteorology than climate and atmospheric chemistry monitoring, is a nadir viewing Michelson interferometer (Clerbaux et al., 2007). The first MetOp satellite was launched in October 2006 (MetOp-A) and IASI was declared operational in July 2007. MetOp is a polar sun-synchronous satellite having descending and ascending nodes at 09:30 and 21:30 LT, respectively. IASI measures in the IR part of the EM spectrum at a horizontal resolution of 12 km at nadir up to 40 km over a swath width of about 2,200 km. IASI covers an infra-red spectral range between 3.7 to 15.4 µm with a total of 8461 spectral channels, out of which 53 channels around 9.6 µm are utilized for ozone retrieval. IASI level 2 ozone products provided by NOAA National Environmental Satellite Data and Information Service (NESDIS) Center for Satellite Application and Research (STAR) are used in this study. The IASI (NOAA/CLASS) ozone product is retrieved based on the AIRS algorithm and has various quality control flags (Table S2). Only QC=0 data which represents a successful IR ozone retrieval is used.

2.1.3 CrIS/ATMS (NUCAPS)

The Cross-track Infrared Sounder (CrIS) and Advanced Technology Microwave Sounder (ATMS) onboard the Suomi NPP satellite were launched in 2011 to feature the high spectral-resolution ("hyperspectral") observations of earth's atmosphere. The CrIS instrument is an advanced Fourier transform spectrometer with an ascending node 13:30 LT and flies at a mean altitude of 824 km and performs fourteen orbits per day. It measures high-resolution IR spectra in the spectral range $650 - 2550$ cm^{-1} with a total of 1305 channels. The ATMS is a microwave sounder with a total of 22 channels ranging from 23 to 183 GHz. These two instruments CrIS and ATMS operate in an

219   overlapping field-of-view (FOV) formation, with ATMS FOVs re-sampled to match the location

220   and size of the 3×3 CrIS FOVs for retrieval under clear to partly cloudy conditions. Here the

221   NUCAPS algorithm-based ozone product of CrIS is utilized. The NOAA Unique CrIS/ATMS

222   Processing System (NUCAPS) is a heritage algorithm developed by the STAR team based on the

223   AIRS retrieval algorithm (Susskind et al., 2003, 2006). The NOAA implemented NUCAPS

224   algorithm is a modular architecture that was specifically designed to be compatible with multiple

225   instruments. The same retrieval algorithms are currently used to process the AIRS/AMSU suite

226   (operations since 2002), the IASI/AMSU/MHS suite (operational since 2008), and now the

227   CrIS/ATMS suite (approved for operations in January 2013). Here again, various quality controls

228   for retrieved data are provided by the NUCAPS science algorithm team, and we used QC=0 for

229   lesser discrepancies in our evaluation. These research products follow a similar retrieval algorithm

230   as developed by the AIRS science team, which gives us further opportunity to assess the AIRS

231   retrieval algorithm for IASI and CrIS radiances.

232

233   **2.1.4 Ozonesonde**

234   Electrochemical concentration cell (ECC) ozonesondes and GPS-radiosondes have been launched

235   from the Aryabhatta Research Institute of Observational Sciences (ARIES) (29.4^o N, 79.5^o E, and

236   1793 m elevation) Nainital (Figure 1), a high-altitude site in central Himalaya, since 2011 (Ojha

237   et al., 2014; Rawat et al., 2020), the only facility in the Himalayan region having regular

238   launchings. ECC ozonesonde relies on the oxidation reaction of ozone with potassium iodide (KI)

239   solution (Komhyr et al., 1967, 1995) to measure ozone partial pressure in the ambient atmosphere.

240   The typical vertical resolution of ozonesonde is about 100 - 150 m and has a precision of better

241   than ± 3 - 5 % with an accuracy of about ± 5 - 10 % up to 30 km altitude under standard operating

242 procedures (Smit et al., 2007). The ozonesonde is connected to iMet-radiosonde via V7 electronic

243 interface where radiosonde consists of GPS, PTU, and a transmitter to transmit signals to the

244 ground. Due to higher accuracy and in-situ measurement, ozonesonde has been widely used

245 worldwide for satellite and model validation (Divakarla et al., 2008; Nassar et al., 2008; Monahan

246 et al., 2007; Kumar et al., 2012a, 2012b; Dufour et al., 2012; Verstraeten et al., 2013; Boynard et

247 al., 2016; Rawat et al., 2020). Both the ascending and descending data were recorded by

248 ozonesonde, however, due to time lag in descending records only ascending data is utilized (Lal

249 et al., 2013, 2014; Ojha et al., 2014). The data is collected at the interval of about 10 meters which

250 is averaged over 100 meters interval using a 3σ filter that removes the outlier values (Srivastava

251 et al., 2015; Naja et al., 2016).

252

253 **2.1.5 Other Auxiliary Data**

254 Additionally, collocated and concurrent OMI and MLS observations are also used to study the

255 tropospheric ozone, UTLS, and total ozone column due to their reasonable sensitivity and well-

256 validated retrievals (Veefkind et al., 2006; Ziemke et al., 2006; Fadnavis et al., 2014; Wang et al.,

257 2021). The tropospheric ozone column obtained from OMI and MLS is based on the residual

258 method, which depends upon the collocated difference between the MLS stratospheric ozone

259 column and OMI total ozone column, which is described in details by Ziemke et al. (2006).

260 Furthermore, the MLS version 4 data is utilized for UTLS column above 261 hPa due to its

261 credibility in this range for scientific applications (Livesey et al., 2013; Schwartz et al., 2015).

262 Moreover, for fair statistical analysis between ozonesonde and MLS ozone profile, a Gaussian

263 smoothing is applied to ozonesonde with full width at half maximum equals to typical upper

264 tropospheric vertical resolution (~ 2 - 4 km) of MLS (Livesey et al., 2013). The best quality data

265   of MLS with data flags, i.e., status=even, quality > 0.6, and convergence < 1.18 is utilized (Ziemke

266   et al., 1998; Barre et al., 2012) is used. However, a slightly different collocation criterion of $3^o \times 3^o$

267   grid box and daytime collocation is utilized for MLS in this work, due to coarser resolution and to

268   get sufficient matchups.

269

270   **2.2 Methods of Analysis**

271   The balloon launch time is mostly around 12:00 IST (Indian Standard Time, which is 5.5 hours

272   ahead of GMT). The Aqua satellite comes over the Indian region around 1:30 pm and 1:30 am

273   IST. Hence for collocation, only noontime (ascending) data (or ± 3 hours of balloon launch) with

274     $1^o \times 1^o$ spatial collocation were chosen in this evaluation. However, for some days, there was no

275   noontime granule in AIRS retrieval (nearly 35 out of total 242 soundings), then we used loose

276   collocation of ±1 day. However, no significant changes were seen after such flexible collocation.

277   Most of the ozonesondes have burst altitudes near 10 hPa, hence AIRS ozone profiles are evaluated

278   from surface to 10 hPa.

279

280   Although suitable collocation criteria have been defined for a fair comparison, still different

281   vertical resolutions of the two data sets (ozonesonde ~100 m and AIRS ~1-5 km) make the

282   meaningful comparison difficult (Smit et al., 2007; Maddy and Barnet 2008). The difference in

283   vertical resolution and retrieval sensitivity has to be accounted for a meaningful comparison.

284   Though there is no perfect way to remove the error arising from the different vertical resolutions

285   of the two measurements, still utilizing the averaging kernel smoothing or Gaussian smoothing,

286   the error is minimized. Various groups have used the satellite averaging kernels smoothing to

287   compare satellite measurements with ozonesonde (Zhang et al., 2010; Verstraeten et al., 2013;

288   Boynard et al., 2016, 2018), while Gaussian smoothing (Wang et al., 2020) and broad layer

289   columns (Nalli et al., 2017) are also utilized. In the present analysis, averaging kernel smoothing

290   is utilized. First, ozonesonde data were interpolated at all AIRS Radiative Transfer Algorithm

291   (RTA) layers from surface to burst altitude, then ozonesonde profiles are smoothed according to

292   the AIRS averaging kernel and a-priori profile (ML climatology), leading to a vertical profile

293   [ozonesonde (AK)] representing what AIRS would have measured for the same ozonesonde

294   sampled atmospheric air mass in the absence of any other error affecting satellite observations.

295   According to Rodgers and Connor (2003), the smoothing of the true state can be characterized as

296   follows:

297    $$X_{est} = X_0 + A`(X_{sonde} - X_0) \qquad (1)$$

298   The AIRS provides averaging kernels information at 9 pressure levels (Figure 2b) whereas the

299   AIRS RTA has 100 pressure levels. So following ozone vertices (Table S3) and formulating

300   trapezoid matrix (Figure 2a, the details regarding the calculation of trapezoid matrices are given

301   in AIRS/AMSU/HSB Version 6 Level 2 Product Levels, Layers and Trapezoids), we convert 9

302   levels AIRS averaging kernels to 100 levels averaging kernels using following defined operation.

303    $$A' = F \times A_{trapezoid} \times F' \qquad (2)$$

304   Where $A_{trapezoid}$ and F are averaging kernel matrices and trapezoid matrices (F' is pseudo-inverse

305   of F). $A_{trapezoid}$ is a given product while F is calculated for given ozone vertices (Table S3).

306

307   Further, in the thermal IR spectrum, the contribution of ozone or any other trace gas towards

308   emission/absorption of IR radiation in the radiative transfer equation depends on the exponent of

309   layer integrated column amounts (Maddy and Barnet, 2008). Hence logarithmic changes in layer

310   column density are more linear than absolute changes. So logarithmic equations are used instead

311   of eq. 1 for smoothing ozonesonde data in the present study.

312    $$\ln (X_{est}) = \ln (X_0) + A'\{\ln (X_{sonde}) - \ln (X_0)\} \qquad (3)$$

313   Where X_{est}, X_{sonde}, and X_0 are smooth ozonesonde or ozonesonde (AK), true ozonesonde, and first

314   guess (ML climatology) profiles, respectively.

315   More details on the calculation of averaging kernels can be found in AIRS documents

316   (AIRS/AMSU/HSB Version 6 Level 2 Product Levels, Layers and Trapezoids) or in available

317   literature (Maddy and Barnet 2008; Irion et al., 2018). A typical averaging kernels matrix and other

318   parameters are shown in Figure 2. Here Figure 2a shows a typical trapezoid matrix, Figure 2b

319   shows the averaging kernels at 9 pressure levels, Figure 2c shows constructed averaging kernels

320   at 100 RTA layers, and Figure 2d shows an example for the different ozone profiles convolved

321   with AKs on 15 June 2011 over the observation site.

322

323   **2.3 Statistical Analysis**

324   The error analysis for AIRS retrieval with interpolated and smoothed ozonesonde is based on Nalli

325   et al. (2013, 2017). Bias, root mean squared error (RMSE), and standard deviation (STD) are

326   studied at various RTA vertical levels from the surface to 10hPa over the Himalayan region. The

327   finer spatio-temporal collocation utilized here has further minimized the uncertainty and error in

328   the evaluation. Since the observation site (29.4º N, 79.5º E) is at a latitude lower than 45º; hence

329   there is a lesser overlap of satellite passes, and mostly a few nadir scans are close to the observation

330   site (mostly daytime granules in range of 75 to 85). Hence all the daytime observations of AIRS

331   are close to ± 3 hours of temporal collocation to the ozonesonde launch and possess a lesser chance

332   of time mismatch.

333

334   Given the collocated ozone mixing ratio profiles for satellite, ozonesonde (AK) and insitu truth

335   (ozonesonde) observations, the statistical errors are calculated as follows -

336

337
$$\text{RMSE } (\Delta O_l) = \sqrt{\frac{\sum_{j=1}^{j=n} W_{l,j} \times (\Delta O_{l,j})^2}{\sum_{j=1}^{j=n} W_{l,j}}} \qquad (4)$$

338

339
$$\text{Bias } (\Delta O_l) = \frac{\sum_{j=1}^{j=n} W_{l,j} \times (\Delta O_{l,j})}{\sum_{j=1}^{j=n} W_{l,j}} \qquad (5)$$

340   Here l runs over different RTA layers and j runs for all collocated profiles, $\Delta O_{l,j}$ the fractional

341   deviation is taken to be the absolute deviation divided by the observed value.

342    $\Delta O_{l,j} = \left(\frac{O^R_{l,j} - O^T_{l,j}}{O^T_{l,j}} \right)$, where O^T and O^R are ozonesonde/ozonesonde (AK) and satellite retrieved

343   ozone mixing ratio respectively.

344    $W_{l,j}$ is the weighting factor and assumes one of three forms $W_0 = 1$, $W_1 = O^R$ and $W_2 = (O^R)^2$ and

345   for ozone to minimize skewing impact due to large variation in mixing ratio at different altitudes,

346   we have used the W_2 weight factor as suggested by other sounder science team (Nalli et al., 2013,

347   2017).

348   The Standard deviation (STD) is then calculated as follows

349

350
$$\text{STD } (\Delta O_l) = \sqrt{[\text{RMSE } (\Delta O_l)]^2 - [\text{Bias } (\Delta O_l)]^2} \qquad (6)$$

351

352　Further to check the strength of the linear relationship between the satellites retrieved data and

353　ozonesonde data the square of Pearson's correlation coefficient is also calculated as follows

354
$$r = \left[\frac{\sum_{j=0}^{j=n} \left(O_j^T - O^T avg\right)\left(O_j^R - O^R avg\right)}{\sqrt{\sum_{j=0}^{j=n}\left(O_j^T - O^T avg\right)^2 \sum_{j=0}^{j=n}\left(O_j^R - O^R avg\right)^2}} \right] \quad (7)$$

355

356　Where the summation is over different pairs of satellite-ozonesonde matchup values.

357

2.4 Estimation of Columnar Ozone

359　The total column ozone (TCO) from ozonesonde is calculated by integrating the ozone mixing

360　ratio from the surface to burst altitude and then adding residual ozone above burst altitude. Here

361　the residual ozone is obtained from satellite-derived balloon-burst climatology (BBC) (McPeters

362　et al., 1997). The discrete integration for calculation of total ozone column (DU) between defined

363　boundaries is performed as follows:

364　$\text{Total column ozone} = 10^7 \times \left(\frac{RT_o}{g_o P_o}\right) \times \sum_{j=1}^{j=n} 0.5 \times (VMR[i] + VMR[i+1]) \times (P[i] - P[i+1])$ (8)

365

366　Where P is ambient pressure in hPa, VMR volume mixing ratio of ozone in ppbv, R (= 287.3 JKg^{-1}K^{-1}) gas constant, g_o (= 9.88 ms^{-2}), P_o (= 1.01325×10^5 Pa) and T_o (= 273.1 K) standard

368　temperature.

369　The UTLS ozone column (DU) is also calculated using Eq. (8), where the UTLS region is defined

370　between 400 hPa to 70 hPa (Bian et al., 2007). Additionally, the tropospheric ozone column (DU)

371　is calculated for ozonesonde utilizing the Eq. (8) with boundaries from the surface to the

372　tropopause. The tropopause height from balloon-borne observations is estimated using the lapse

373　rate method as well as the AIRS-derived tropopause is used and shown in Figure 3. However for

374   OMI and MLS tropospheric ozone residual method is used which calculates the tropospheric ozone

375   column by subtracting the OMI total column from MLS stratospheric ozone column (Hudson et

376   al., 1998; Ziemke et al., 2006).

377

378   **3. Results and Discussion**

379   **3.1 Ozone Distribution along Balloon Trajectory: Ozonesonde and AIRS**

380   The distributions of ozone along the balloon tracks obtained using all ozone soundings data during

381   four seasons are shown in Figure 4. The nearest swath of AIRS ozone observations is interpolated

382   to the balloon locations and altitude are also shown. Altitude variations of the balloon along

383   longitude is shown in Figure S3. The balloons drift to a very long distance during winter followed

384   by autumn and spring. During these seasons, often balloons reach Nepal also. The wind reversal

385   takes place during the summer-monsoon when the balloon drifted towards IGP regions (Figure 4).

386   The distributions of ozone from AIRS are more or less similar to the distributions those from

387   ozonesonde. This ozone variation reflects is term of spatial as well as vertical distributions. The

388   bias and coefficient of determination (r^2) between ozonesonde and AIRS ozone is studied along

389   the longitude and latitude (Figures S3 and S4). Lower biases (lesser than 10%) and higher r^2 are

390   seen in the lower and middle troposphere. The poor correlation (<0.4) and larger biases of up to

391   28% are seen at certain longitudes those are associated with higher altitudes (> 20 km). Around

392   the balloon launch site (Nainital, 79.45 E) highest r^2 score of 0.98 and low bias of 1.4% is observed,

393   which remain higher (r^2) and lower (bias) up to 80° E (Figure S3).

394

395

396

3.2 Ozone Soundings and AIRS Ozone Profiles

Figure 5 shows the average monthly ozone profiles for collocated observations of ozonesonde and AIRS, respectively, during seven-year periods. The ozonesonde convolved with AIRS averaging kernels [ozonesonde (AK)] and AIRS a priori are also compared. The value of percentage difference between ozonesonde and AIRS ozone at 706, 617, 496, 103, 29, and 14 hPa altitudes are shown in the figure 5 and the zoomed variations in the lower tropospheric ozone (surface to 200 hPa) are also presented in the insets. AIRS slightly (~10%) underestimate ozone in the lower troposphere during most of the months, except the summer-monsoon (June-August), where an overestimation of up to 20% is observed. In the middle troposphere, around 300 hPa, an underestimation in the range 1 - 17% is seen for all months with an approaching tendency of ozonesonde (AK) towards the true ozonesonde profiles. However, near the tropopause region, AIRS retrievals considerably overestimate ozone by up to 102%. The overestimation was the highest for the winter season (82 - 102%), followed by the spring, autumn, and the lowest for the summer-monsoon season (10 - 27%). In the stratosphere, where the sensitivity of AIRS is higher (Figure 2c), the ozonesonde and AIRS differences were relatively lower with an underestimation in between 5 - 21%.

As expected, the difference between ozonesonde and AIRS is significantly reduced (Table 1) after applying the averaging kernel or accounting for the sensitivity difference. This reduction was more notable for the summer monsoon period near the tropopause, where the difference reduced from 92% to 19%, providing improvement by 72%. The improvement is as high as 100% on monthly basis. Additionally, relative difference profiles were also analyzed for individual soundings as well for the different seasons (Figure S5). Higher differences of about 150% between AIRS and

420 ozonesonde ozone observations were seen in the upper troposphere and lower stratospheric

421 (UTLS) region. The higher difference during winter and spring between these observations in the

422 UTLS region could be due to recurring ozone transport via tropopause folding over the observation

423 site. Such events may remain undetected by AIRS due to lower vertical resolution leading to

424 missing of some tropopause folding events at lower altitudes (Figure 3). However, in the lower

425 troposphere, larger differences between ozonesonde and AIRS during summer-monsoon are seen,

426 which are due to low ozone and frequent cloudy conditions leading to poor retrieval. The arrival

427 of cleaner oceanic air during south-west monsoon (or summer monsoon) brings ozone poor air and

428 frequent cloudy conditions over the northern India that weakens the photochemical ozone

429 production (Naja et al., 2014; Sarangi et al., 2014). Moreover, in the lower troposphere the limited

430 sensitivity of hyperspectral satellite instruments has significant contribution from the a priori

431 information, which is also observed for AIRS retrieval (Figure 5).

432

433 Figure 6 shows the yearly time series analysis of average ozone mixing ratio at four defined layers,

434 characterizing the middle troposphere (600 - 300 hPa), the upper troposphere (300 - 100 hPa),

435 lower stratosphere (100 - 50 hPa), and middle stratosphere (50 - 10 hPa) respectively. A prominent

436 seasonality was seen in the time series throughout the years, which is quite clear in the upper

437 troposphere (300 - 100 hPa). The ozone seasonality contrast reflects the influence of summer-

438 monsoon and winter seasons. The seasonality contrast is similar between AIRS and ozonesonde

439 measurements, while a reversal of ozone seasonality is observed in the middle stratospheric region

440 compared to other layers. The opposite seasonality of the middle stratospheric region is primarily

441 due to dominant circulations, variation of solar radiation and dynamics. Total column water vapor

442 and monsoon index is also shown in Figure 6 and both show a tendency of anti-correlation with

443 ozone in 300 - 100 hPa region. The monsoon index is estimated (Wang et al., 2001) by the

444 difference between zonal (U) wind (MERRA-2) at 850 hPa over the Arabian Sea (40 E – 80 E, 5

445 N – 15 N) and over the central Indian landmass (70 E - 90 E, 20 N – 30 N). The anti-correlation

446 with total column water vapor is slightly higher for AIRS ozone (~0.26) and it is somewhat lower

447 with ozonesonde (~0.15) in 300-100 hPa region. The relative difference of AIRS ozone with

448 ozonesonde in the upper tropospheric region also shows an anti-correlation (Figure S6) of 0.17

449 with total column water vapor and of 0.27 with monsoon index, respectively.

450

451 In general, the positive values of the monsoon index correspond to strong monsoon, and negative

452 values correspond to weak monsoon periods (Wang et al., 2001). During the weak monsoon, there

453 is relatively drier air, lower cloud cover and higher surface temperature compared to the strong

454 monsoon period (Lu et al., 2018). We observed an anti-correlation (-0.49) between yearly average

455 ozone and monsoon index. Furthermore, the larger ozone differences between AIRS and

456 ozonesonde is associated with the lower water vapor, which may be arising due to the influence of

457 ozone-sensitive water vapor (WV) channels in mid-Infra-red regions. Further, in the middle

458 troposphere (600-300 hPa), a secondary ozone peak in post-monsoon is observed, which is

459 suggested to be influenced by the biomass burning (Figure S7) over northern India that seems to

460 be missing in the AIRS ozone.

461

462 In the middle troposphere (600 - 300 hPa) and lower stratosphere (100 - 50 hPa), AIRS retrievals

463 show higher differences with respect to ozonesondes, while a nominal difference is observed for

464 middle troposphere and middle stratosphere. (Figure S6). Furthermore, a systematic increase of

465 standard deviation is also seen with the altitude. The higher standard deviations in the upper

466 tropospheric and stratospheric regions are mainly due to higher ozone variability associated with

467 stratosphere-troposphere exchange (STE) processes over the Himalayan region (Naja et al., 2016;

468 Bhardwaj et al., 2018).

469

3.3 Statistical Analysis of AIRS Ozone Profiles

471 Error analysis of AIRS retrieved ozone over the Himalayan region is performed with spatio-

472 temporal collocated ozonesonde observations as a reference. The methodology to calculate the

473 root mean square error (RMSE), bias, and standard deviation (STD) is described in section 2.3.

474 W_2 weighting statistics is utilized due to abrupt changes of atmospheric ozone with altitude. Here

475 bias and STD between AIRS and ozonesonde are calculated at different RTA layers from surface

476 to 10 hPa. Figure 7 shows the average variation of bias and STD at different RTA layers from

477 surface to 10 hPa over this region. The mean biases between ozonesonde and MLS, a high vertical

478 resolution satellite instrument, is also shown in figure 7. In general, higher positive bias (~65%)

479 and STD (~25%) in AIRS ozone is seen in the UTLS region, where MLS agrees well with

480 ozonesonde. In the lower and middle troposphere, the AIRS ozone retrieval is negatively biased

481 (0 - 25%), which increases gradually from the surface to higher altitudes (~ 350hPa). A negative

482 bias was also seen in the stratosphere of about 15%. Similar to the bias, STD are also smaller in

483 the lower troposphere and stratosphere with values of nearly 15%. The higher statistical errors in

484 the upper troposphere and the lower stratospheric region could be due to lower ozone partial

485 pressure and frequent stratospheric to tropospheric transport events over the Himalayas (Rawat et

486 al., 2020, 2021), which introduces error either after mismatch of events in AIRS coarser vertical

487 resolution or due to complex topography. Additionally, the AIRS tropopause frequency

488 distribution shows less ability of AIRS to capture deep intrusion events (Figure 3). Further, AIRS

489   trace gas retrieval largely depends on successful temperature retrieval and uses temperature

490   retrieval as an input parameter (Maddy and Barnet 2008). Hence, temperature retrieval error could

491   also propagate to ozone, and statistical error analysis of AIRS temperature shows relatively higher

492   biases (~ 2 K) in the upper tropospheric region (Figure S8).

493

494   The statistical error analysis was more or less similar for both true and smoothed ozonesonde

495   profiles. However, notable reduction in tropospheric bias and vertical shifts of errors were also

496   observed after applying the averaging kernel matrix to the true ozonesonde throughout the profile.

497   A shift of the error peak is seen from the lower stratosphere to the upper troposphere. This could

498   be due to the higher sensitivity of AIRS retrieval in the lower stratosphere, which would have

499   minimized the error at these particular altitudes. However, in the upper troposphere, higher

500   contribution of a-priories as well as other factors (i.e., STE) might have resulted in larger biases

501   and errors.

502

503   The histogram of differences between AIRS and ozonesonde (AK) is also studied at various

504   defined layers (Figure 8). AIRS mostly underestimates ozone with a mean bias of 2.37 ppbv, 9.29

505   ppbv, and 39.8 ppbv in 800 - 600 hPa, 600 - 300 hPa, and 100 - 50 hPa layers, respectively, while

506   in the upper troposphere (300 - 100 hPa) AIRS overestimated with a mean bias of 43.22 ppbv.

507   Furthermore, distributions of differences are skewed towards the negative values in the lower

508   stratosphere and towards positive values in the upper troposphere. More symmetric distribution

509   over the negative axis is observed in the middle and lower troposphere. We also studied the

510   correlation profiles for different seasons (Figure 8 right panel). A strong correlation is seen in the

511   lower and middle troposphere for spring and summer, while a poor correlation for winter and

512   autumn. In the lower troposphere, a larger difference between AIRS and ozonesonde(AK) is

513   observed particularly during summer, with relatively higher correlation mostly due to greater

514   concurrence of a-priori with ozonesonde(AK). Whereas, in the upper troposphere (300 - 100 hPa)

515   a larger difference during winter and spring is primarily due to frequent subtropical dynamics,

516   while a higher correlation during the winter is mainly contributed from the AIRS retrieval.

517   Furthermore, the correlation coefficient between AIRS and ozonesonde shows a higher value in

518   the middle stratosphere (0.95) and lower stratosphere (0.92), followed by in the upper troposphere

519   (0.68), the lower troposphere (0.62), and middle troposphere (0.47).

520

521   **3.4 Assessment of AIRS Retrieval Algorithm with IASI and CrIS Radiance**

522   The MetOp/IASI and Soumi-NPP/CrIS radiance-based ozone products are assessed using

523   ozonesonde data over the central Himalayan region for one year (April 2014 to April 2015),

524   utilizing a total of 32 soundings. Here, the IASI and CrIS based ozone retrievals are research

525   products provided by NOAA, whose retrieval is based on the AIRS retrieval algorithm and follows

526   a similar averaging kernels (Nalli et al., 2017). For IASI, due to the 09:30 ascending nodes

527   (morning overpass in India), ±6 h loose temporal collocation is used. However, CrIS and AIRS

528   follow the same collocation due to a similar noontime overpass. The IASI, CrIS, and AIRS sensors

529   have 8461, 1305, and 2378 IR channels respectively. Hence, analyzing their satellite ozone

530   products further helps to assess the AIRS retrieval algorithm for different IR radiances and channel

531   sets.

532

533   Figure 9a shows the seasonal ozone profiles obtained from three IR satellite sensors along with

534   ozonesonde for one year period. All sensors showed more-or-less similar ozone peak altitude and

535 ozone gradient. The estimated ozone peak altitude for ozonesonde, AIRS, IASI and CrIS are 11.35

536 hPa, 10 hPa, 9.11 hPa, and 7.78 hPa, respectively. The estimated annual average ozone gradient

537 in regions between tropopause to gradient peak are 231.5 ppbv/hPa, 199.0 ppbv/hPa, 193.2

538 ppbv/hPa and 199.1 ppbv/hPa for ozonesonde, AIRS, CrIS, and IASI, respectively.

539

540 Higher ozone concentrations during spring throughout the troposphere are captured well by all

541 satellite sensors. Higher ozone during spring and winter in the UTLS region are observed by AIRS

542 and IASI similar to ozonesonde but not by CrIS. At the same time, CrIS sensitivity looks relatively

543 low, where the possible role of the number of channels can be seen. However, IASI and AIRS

544 have effectively captured the ozone seasonal variability.

545

546 Figure 9b shows the weighted statistical error analysis of IASI, CrIS, and AIRS ozone retrieval

547 with the true ozonesonde observations. Here, the difference in sensitivity of the two data sets is

548 not accounted for as this section's primary aim is to assess the AIRS retrieved algorithm using

549 different IR sensor radiances and channel sets. All three space-borne sensors overestimated UTLS

550 ozone by more than 50%, however, in the stratosphere and lower troposphere, the bias was slightly

551 lower and it is somewhat underestimated. Similar to bias the STD were also higher in the UTLS

552 region by more than 60%. A consistent larger error in the UTLS region for three IR satellite sensors

553 that share the same radiative transfer model and retrieval algorithm shows the possible influence

554 of complex topography and the various STE processes in introducing errors in retrieval processes,

555 apart from input a-priories of the retrieval.

556

557   Additionally, Pearson correlations between ozonesonde and IASI, CrIS, and AIRS are also studied

558   at five atmospheric layers (i.e., 600-800 hPa, 300-600 hPa, 100-300 hPa, 50-100 hPa, and 10 - 50

559   hPa) (Table 2). A relatively stronger positive correlation is found in the middle stratosphere (50-

560   100 hPa) and lower stratosphere (50 - 100 hPa), which was highest for AIRS followed by CrIS

561   and IASI, and a relatively low correlation is observed in the middle troposphere (300-600 hPa) for

562   AIRS and IASI (~ 44% and 31%), while CrIS shows the poor correlation in the lower troposphere

563   about 9%. The lower concurrence between ozonesonde and the satellite sensors in the lower

564   troposphere could be due to lower sensitivity and shorter life time of near surface ozone that could

565   increase the a priori contribution and sampling mismatch, respectively.

566

567   **3.5 Columnar Ozone**

568   **3.5.1 Total Column Ozone (TCO)**

569   Figure 10a shows variations in monthly average total column ozone (TCO) from ozonesonde,

570   AIRS, and OMI during 2011 - 2017. Here the box plots are also overlaid on mean column to

571   describe the distribution of monthly column data. In general, the TCO is higher during spring,

572   which subsequently drops in summer-monsoon. AIRS TCO shows a bimodal monthly variation

573   which is not seen in the ozonesonde and OMI observations, otherwise its monthly variation is in

574   reasonable agreement with ozonesonde. The OMI TCO are in good match with the ozonesonde

575   with a maximum difference of up to about 5 DU. Table 3 shows the difference in the TCO between

576   AIRS, OMI, and ozonesonde. AIRS shows considerable overestimation in the range of 2.2 - 22

577   DU for some months while notable underestimation (1.8 - 4 DU) for others, with respect to both

578   ozonesonde and OMI. The correlation between AIRS TCO and ozonesonde TCO is found to be

579   0.5 (Table S4). To further understand the cause of bimodal variations in AIRS (higher ozone during

580   August, September, and October), the AIRS ozone profiles were integrated between different

581   stratospheric region (100 – 70 hPa, 70 - 50 hPa, 50 - 20 hPa and 20 – 1 hPa) and we found that the

582   elevated total ozone during post-monsoon is mainly contributed from the altitude above 50 hPa.

583

584   **3.5.2 UTLS Ozone Column**

585   Figure 10b shows the variations in monthly average UTLS ozone column for collocated and

586   concurrent observations of AIRS, MLS, and ozonesonde during 2011 - 2017. The UTLS region

587   extends between 400 hPa to 70 hPa (Bian et al., 2007) for ozonesonde and AIRS, while for MLS

588   region between 261 hPa to 70 hPa is utilized. The recommended pressure levels for MLS v4 ozone

589   retrieval is above 261 hPa (Livesey et al., 2013; Schwartz et al., 2015). In contrast to TCO, a higher

590   ozone in UTLS is seen during the winter and spring (~ 45 DU) when there are recurring downward

591   transport events, while a clear drop of the column during the summer-monsoon shows the

592   convective transport of cleaner oceanic air to the higher altitudes. All the collocated observations

593   are able to capture the monthly variation effectively; however, there is a substantial overestimation

594   by more than 3 DU (Table S5) for all the months in AIRS measurements, while MLS mostly

595   underestimate except during winter due to smaller integrated columns. Further, the larger whiskers

596   of box plot during winter and spring show the larger variations of the ozone in the UTLS region.

597   Though there were notable overestimations compared to ozonesonde, still UTLS monthly

598   variations are captured well by AIRS with a correlation of up to 75% (Table S4). In addition the

599   correlation of ozonesonde and AIRS ozone at each pressure levels in UTLS region is 0.81, which

600   further increases with ozonesonde(AK) (of about 0.94). The persistent biases in the satellite

601   retrievals arises due to inadequate input parameters that can be improved by using more accurate

602   initial parameters and surface emissivity (Dufour et al., 2012; Boynard et al., 2018).

3.5.3 Tropospheric Ozone Column

Figure 10c shows the variations in monthly average tropospheric ozone column utilizing various collocated data sets during 2011 - 2017. The tropospheric ozone column is calculated by integrating ozone profiles from the surface to the tropopause. WMO-defined lapse rate calculation method is used to calculate tropopause height from balloon-borne and AIRS observations (Figure 3). Higher tropospheric ozone is observed during the spring and early summer (> 45 DU) when annual crop-residue burning (Figure S7) events occur over northern India, apart from downward transport from the stratosphere. Few cases of downward transport are discussed in the next section. The tropospheric ozone column drops rapidly during the summer-monsoon when pristine marine air reaches Nainital. A slight increase of column is also seen during the autumn, which is again influenced by post-monsoon crop residue burning practices (Figure S7) in northern India (Bhardwaj et al., 2016). The AIRS is able to capture the monthly variations very effectively; however, there are larger biases. The biases with ozonesonde are higher when the tropopause is taken from the balloon-borne observation, while with AIRS provided tropopause, the biases are lesser or mostly within the one sigma limit. The correlation between ozonesonde and AIRS, when used AIRS tropopause, is very strong (0.72). Like AIRS, the OMI/MLS column is in good agreement and able to produce monthly variations; however, there are larger differences during winter and spring of more than 10 DU. The tropospheric ozone column from ozonesonde is different for balloon-borne LRT and AIRS tropopause, whose possible reason could be due to the lower vertical resolution of AIRS, which calculates tropopause with an uncertainty of 1-2 km (Divakarla et al., 2006), and on average a lower tropopause pressure (or higher altitude) by 28% is calculated by AIRS compare to ozonesonde measurements (Figure 3).

3.6 Case Studies of Biomass Burning and Downward Transport

Over the northern India, extensive agriculture practices and forest fires influence ozone at the surface and higher altitudes (Kumar et al., 2011; Cristofanelli et al., 2014; Bhardwaj et al., 2016; Bhardwaj et al., 2018). Based on MODIS fire counts, the days in between 1 March to 15 April over northern India are classified as the low fire periods (LFP) as considered in previous studies over this region. The high fire period (HFP) is classified when the fire counts over the observational site are more than the median fire counts in the biomass burning period, typically from mid-April to May (Bhardwaj et al., 2016). A total of 32 soundings (mid-April to May) are classified as HFP and 33 soundings (March to mid-April) are classified as LFP. Figure 11 (left) shows the average ozone profiles up to 6 km from ozonesonde and AIRS observations during HFP and LFP. The ozonesonde data show enhancement in ozone by about 5 ppbv to about 11 ppbv during HFP as compared to LFP that is accounting to 5-20% increase. It is important to mention that enhancement is greater at higher altitude region. The enhancement is slightly lower (10-15%) in AIRS profile, where most of it is contributed by the a priori profile (Figure S8).

Deep stratospheric intrusion or the downward transport (DT) of ozone-rich air from the stratosphere to the troposphere significantly influences ozone profiles over the subtropical regions (Collins, et al., 2003; Zhu, et al., 2006; Lal et al., 2014). Over the subtropical Himalayas, such ozone intrusions are observed during the winter and the spring seasons (Zhu et al., 2006; Ojha et al., 2014). The DT events are classified based on the higher ozone in middle - upper troposphere seen from ozonesonde with relatively larger Ertel potential vorticity (EPV) and lower humidity in MERRA-2 reanalysis data. Based on this, 10 soundings (between January and mid-April) are classified as DT events for ozonesonde and AIRS. Figure 11 (right) shows ozone profiles from

649   ozonesonde (AK) and AIRS observations for high ozone DT events as well as the average ozone

650   profiles of corresponding months excluding the DT event. Though there are persistent positive

651   biases in AIRS ozone profile compared to ozonesonde in the middle/upper troposphere, still both

652   the observations have captured the influence of the downward transport on the ozone profile very

653   effectively and show an increase in ozone of 10 - 20% in altitude range 2 - 16 km. Ozonesonde

654   based observations have shown about two fold increase in upper-middle tropospheric ozone due

655   to downward ozone transport over this region (Ojha et al., 2014). Further, the first guess profile's

656   contribution to AIRS retrieval during DTs is negligible (Figure S9) and shows main contribution

657   from the observations itself. So despite the persistent biases in the AIRS and ozonesonde

658   observations, AIRS is able to capture the influences of downward transport (DT) on ozone profile

659   notably well.

660

661   **3.7 Ozone Radiative Forcing**

662   Radiative forcing is a valuable metric to estimate the radiative impacts of any anthropogenic or

663   natural activity on the climate system (Ramaswamy et al., 2001). It measures the net radiation at

664   the surface, tropopause, and the top of the atmosphere due to any atmospheric constituents. Here

665   we discuss the ozone radiative forcing (RF) at the surface in the ultraviolet (UV) spectral range

666   (Antón et al., 2014; Mateos et al., 2020) using the ozonesonde, OMI, and AIRS total column ozone

667   (TCO) data. The RF is calculated based on Antón et al. (2014), relative to 1979 utilizing TOMS

668   TOC data in 1979, monthly averaged solar zenith angles of site, clearness index based on

669   Chakraborty et al., (2014) and Hawas et al., (1984), and respective monthly average TCO data of

670   AIRS, OMI, and ozonesonde. Rather than quantifying the RF values here, our primary focus is to

671   show how the discrepancies of satellite ozone data (mainly AIRS) can impact the calculation of

672 RF values. Figure 12 shows the seasonal average ozone radiative forcing (RF) relative to 1979.

673 The annual average ozone RF during 2011 -2017 is 4.86, 4.04, and 2.96 mW/m^2 for ozonesonde,

674 OMI, and AIRS, respectively. The RF values for ozonesonde and OMI are comparable to Mateos

675 et al. (2020) (4 mW/m^2) for the extratropical region. However, for AIRS, the RF value is lower by

676 45%. Further, the seasonal average ozone RF (2011-2017) is consistent between ozonesonde and

677 OMI, while notable differences are seen in AIRS except during the winter season when differences

678 are marginal (Figure 12). Also from Table 3, it is clear that the higher total ozone bias during

679 autumn (as high as 22 DU) contributes to higher RF differences in autumn (Figure 12).

680

681 **4. Summary and Conclusions**

682 This study has utilized 242 ozone soundings (during 2011 - 2017) conducted over the Himalayan

683 station (Nainital) to evaluate the AIRS version 6 ozone product and study the performance during

684 biomass burning events, ozone downward transport events and estimation of ozone radiative

685 forcing. AIRS ozone retrieval is evaluated in terms of retrieval sensitivity, retrieval biases, retrieval

686 errors, and ability to retrieve the natural variability of columnar ozone at different altitude regions.

687 This study is first of its kind in the Himalayan region. The AIRS averaging kernels information

688 was applied to ozonesonde for a like-for-like comparison to overcome their sensitivity differences.

689 The monthly profile evaluation shows ozone peak and ozone altitude dependency is captured well

690 by AIRS retrieval with smaller but notable underestimation (5 - 20%) in the lower-middle

691 troposphere and stratosphere, while overestimation in the UTLS region as high as 102%. We show

692 the larger sensitivity of AIRS ozone for the summer monsoon in the UTLS region, where the biases

693 between AIRS and ozonesonde improved remarkably after applying AIRS averaging kernel

694 information.

695   The weighted statistical error analysis of AIRS retrieved ozone profiles shows higher positive

696   biases (65%) and STD (25%) in the upper troposphere. In the lower and middle troposphere, AIRS

697   ozone was negatively biased, apart from the stratosphere. In addition, though the biases and errors

698   are higher in the upper troposphere, there is a larger correlation of about 81% showing the

699   capability of AIRS to retrieve upper tropospheric ozone variability with certain positive biases that

700   can be eliminated by choosing better emissivity inputs or other retrieval inputs. The AIRS ozone

701   retrieval algorithm was further evaluated using the radiance of IASI and CrIS sensors; these

702   sensors provided similar error statistics as seen for AIRS.

703

704   The AIRS-derived columnar ozone amounts (i.e., total, UTLS, and tropospheric ozone) are also

705   evaluated to see whether the ozone variability at different altitude regions is being retrieved

706   correctly. The UTLS and tropospheric ozone monthly variations are captured well by AIRS with

707   persistence positive biases. However, the total ozone column shows bimodal monthly variations,

708   which was not evident in the ozonesonde and OMI total ozone observations. Further, we found

709   higher total ozone column in AIRS during autumn, which is mostly coming from the stratospheric

710   region above 50 hPa. The capabilities of AIRS to capture various biomass burning and downward

711   transport events have also been studied. AIRS captures all such events reasonably well with

712   notable contributions of the a priori, particularly in the biomass burning events.

713

714   Unlike the well-mixed greenhouse gases, the ozone radiative forcing (RF) remains uncertain due

715   to inadequate budget estimates and complex chemical processes. The total ozone discrepancies of

716   AIRS lead to show lower RF (by about 45%) and greater uncertainty in this Himalayan region.

717   Stevenson et al. (2013) have shown that a few percent uncertainties in ozone concentrations can

718 produce a spread of ~17% in ozone RF estimations. Here, the role of in-situ observations from

719 ozone soundings is shown to be important in improving the satellite retrieved ozone over the

720 Himalayan region by assessing and providing insights upon its error and bias. This information

721 could be applied for the ozone product from other satellite data set, having long-term coverage.

722 This will help in better understanding regional ozone and radiation budgets over this Himalayan

723 region having complex topography.

724

737

738

739 **Data availability:** Satellite data are available in the respective web portal. Ozonesonde data could

740 be made available on a reasonable request by writing to the corresponding author.

References

741

Antón, M., D. Mateos, R. Román, A. Valenzuela, L. Alados-Arboledas, and F. J. Olmo.: A method

to determine the ozone radiative forcing in the ultra-violet range from experimental data, J.

Geophys. Res. Atmos., 119, 1860–1873, doi:10.1002/2013JD020444, 2014.

Aghedo, A.M., Bowman, K.W., Worden, H.M., Kulawik, S.S., Shindell, D.T., Lamarque, J.F.,

Faluvegi, G., Parrington, M., Jones, D.B.A. and Rast, S.: The vertical distribution of ozone

instantaneous radiative forcing from satellite and chemistry climate models. Journal of

Geophysical Research: Atmospheres, 116(D1), 2011.

Bai, W., Wu, C., Li, J. and Wang, W.: Impact of terrain altitude and cloud height on ozone remote

sensing from satellite, Journal of Atmospheric and Oceanic Technology, 31(4), pp.903-912, 2014.

Barre, J., Peuch, V.H., Attié, J.L., Amraoui, L.E., Lahoz, W.A., Josse, B., Claeyman, M. and

Nedelec, P.: Stratosphere-troposphere ozone exchange from high resolution MLS ozone analyses,

Atmos. Chem. Phys., 12(14), pp.6129-6144, 2012.

Bhardwaj, P., Naja, M., Kumar, R. and Chandola, H.C.: Seasonal, interannual, and long-term

variabilities in biomass burning activity over South Asia, Environmental Science and Pollution

Research, 23(5), pp.4397-4410, 2016.

Bhardwaj, P., Naja, M., Rupakheti, M., Lupascu, A., Mues, A., Panday, A. K., Kumar, R., Mahata,

K. S., Lal, S., Chandola, H. C., and Lawrence, M. G.: Variations in surface ozone and carbon

monoxide in the Kathmandu Valley and surrounding broader regions during SusKat-ABC field

765 campaign: role of local and regional sources, Atmos. Chem. Phys., 18, 11949–11971,

766 https://doi.org/10.5194/acp-18-11949-2018, 2018.

767

768 Bhartia, P.K., McPeters, R.D., Mateer, C.L., Flynn, L.E. and Wellemeyer, C.: Algorithm for the

769 estimation of vertical ozone profiles from the backscattered ultraviolet technique, J. Geophys. Res.

770 Atmos., 101(D13), pp.18793-18806, 1996.

771

772 Bian, J., Gettelman, A., Chen, H. and Pan, L.L.: Validation of satellite ozone profile retrievals

773 using Beijing ozonesonde data, J. Geophys. Res. Atmos., 112(D6), 2007.

774

775 Boynard, A., Hurtmans, D., Koukouli, M.E., Goutail, F., Bureau, J., Safieddine, S., Lerot, C.,

776 Hadji-Lazaro, J., Wespes, C., Pommereau, J.P. and Pazmino, A.: Seven years of IASI ozone

777 retrievals from FORLI: validation with independent total column and vertical profile

778 measurements, Atmos. Meas. Tech., 9(9), pp.4327-4353, 2016.

779

780 Boynard, A., Hurtmans, D., Garane, K., Goutail, F., Hadji-Lazaro, J., Koukouli, M. E., Wespes,

781 C., Vigouroux, C., Keppens, A., Pommereau, J.-P., Pazmino, A., Balis, D., Loyola, D., Valks, P.,

782 Sussmann, R., Smale, D., Coheur, P.-F., and Clerbaux, C.: Validation of the IASI

783 FORLI/EUMETSAT ozone products using satellite (GOME-2), ground-based (Brewer–Dobson,

784 SAOZ, FTIR) and ozonesonde measurements, Atmos. Meas. Tech., 11, 5125–5152,

785 https://doi.org/10.5194/amt-11-5125-2018, 2018.

786 Chakraborty, S., Sadhu, P.K. and Nitai, P.A.L.: New location selection criterions for solar PV

787 power plant. International Journal of Renewable Energy Research, 4(4), pp.1020-1030, 2014.

788

789 Clerbaux, C., Hadji-Lazaro, J., Turquety, S., George, M., Coheur, P.F., Hurtmans, D., Wespes, C.,

790 Herbin, H., Blumstein, D., Tourniers, B. and Phulpin, T.: The IASI/MetOp1 Mission: First

791 observations and highlights of its potential contribution to GMES2, Space Research Today, 168,

792 pp.19-24, 2007.

793

794 Coheur, P.F., Barret, B., Turquety, S., Hurtmans, D., Hadji- Lazaro, J. and Clerbaux, C.: Retrieval

795 and characterization of ozone vertical profiles from a thermal infrared nadir sounder, J. Geophys.

796 Res. Atmos., 110(D24), 2005.

797

798 Collins, W. J., R. G. Derwent, B. Garnier, C. E. Johnson, M. G. Sanderson, and D. S. Stevenson.:

799 Effect of stratosphere-troposphere exchange on the future tropospheric ozone trend, J. Geophys.

800 Res., 108(D12), 8528, doi:10.1029/2002JD002617, 2003.

801

802 Cristofanelli, P., Putero, D., Adhikary, B., Landi, T.C., Marinoni, A., Duchi, R., Calzolari, F., Laj,

803 P., Stocchi, P., Verza, G. and Vuillermoz, E.: Transport of short-lived climate forcers/pollutants

804 (SLCF/P) to the Himalayas during the South Asian summer monsoon onset, Environmental

805 Research Letters, 9(8), p.084005, 2014.

806

807 Divakarla, M., Barnet, C., Goldberg, M., Maddy, E., Wolf, W., Flynn, L., Xiong, X., Wei, J., Zhou,

808 L. and Liu, X.: Validation of Atmospheric Infrared Sounder (AIRS) temperature, water vapor, and

809 ozone retrievals with matched radiosonde and ozonesonde measurements and forecasts, In

810   Multispectral, Hyperspectral, and Ultraspectral Remote Sensing Technology, Techniques, and

811   Applications, International Society for Optics and Photonics, Vol. 6405, p. 640503, 2006.

812

813   Divakarla, M., Barnet, C., Goldberg, M., Maddy, E., Irion, F., Newchurch, M., Liu, X., Wolf, W.,

814   Flynn, L., Labow, G. and Xiong, X.: Evaluation of Atmospheric Infrared Sounder ozone profiles

815   and total ozone retrievals with matched ozonesonde measurements, ECMWF ozone data, and

816   Ozone Monitoring Instrument retrievals, J. Geophys. Res. Atmos., 113(D15), 2008.

817

818   Dufour, G., Eremenko, M., Griesfeller, A., Barret, B., LeFlochmoën, E., Clerbaux, C., Hadji-

819   Lazaro, J., Coheur, P.F. and Hurtmans, D.: Validation of three different scientific ozone products

820   retrieved from IASI spectra using ozonesondes, Atmos. Meas. Tech., 5(3), pp.611-630, 2012.

821

822   Ebi, K.L. and McGregor, G., Climate change, tropospheric ozone and particulate matter, and health

823   impacts, Environmental health perspectives, 116(11), pp.1449-1455, 2008.

824

825   Fadnavis, S., Dhomse, S., Ghude, S., Iyer, U., Buchunde, P., Sonbawne, S. and Raj, P.E.: Ozone

826   trends in the vertical structure of Upper Troposphere and Lower stratosphere over the Indian

827   monsoon region, International Journal of Environmental Science and Technology, 11(2), pp.529-

828   542, 2014.

829

830   Fishbein, E., Farmer, C.B., Granger, S.L., Gregorich, D.T., Gunson, M.R., Hannon, S.E.,

831   Hofstadter, M.D., Lee, S.Y., Leroy, S.S. and Strow, L.L.: Formulation and validation of simulated

832   data for the Atmospheric Infrared Sounder (AIRS), IEEE Transactions on Geoscience and Remote

833   Sensing, 41(2), pp.314-329, 2003.

834

835   Foret, G., Eremenko, M., Cuesta, J., Sellitto, P., Barré, J., Gaubert, B., Coman, A., Dufour, G.,

836   Liu, X., Joly, M. and Doche, C.: Ozone pollution: What can we see from space? A case study, J.

837   Geophys. Res. Atmos., 119(13), pp.8476-8499, 2014.

838

839   Forster, P.M., Bodeker, G., Schofield, R., Solomon, S. and Thompson, D.: Effects of ozone cooling

840   in the tropical lower stratosphere and upper troposphere, Geophysical Research Letters, 34(23),

841   2007.

842

843   Finlayson-Pitts, B.J. and Pitts, J.N.: Tropospheric air pollution: ozone, airborne toxics, polycyclic

844   aromatic hydrocarbons, and particles, Science, 276(5315), pp.1045-1051, 1997.

845

846   Fishman, J., Ramanathan, V., Crutzen, P.J. and Liu, S.C.: Tropospheric ozone and climate, Nature,

847   282(5741), pp.818-820, 1979.

848

849   Fishman, J., Minnis, P. and Reichle Jr, H.G.: Use of satellite data to study tropospheric ozone in

850   the tropics, J. Geophys. Res. Atmos., 91(D13), pp.14451-14465, 1986.

851

852   Fishman, J. and Larsen, J.C.: Distribution of total ozone and stratospheric ozone in the tropics:

853   Implications for the distribution of tropospheric ozone, J. Geophys. Res. Atmos., 92(D6), pp.6627-

854   6634, 1987.

855

856 Gauss, M., Myhre, G., Pitari, G., Prather, M.J., Isaksen, I.S.A., Berntsen, T.K., Brasseur, G.P.,

857 Dentener, F.J., Derwent, R.G., Hauglustaine, D.A. and Horowitz, L.W.: Radiative forcing in the

858 21st century due to ozone changes in the troposphere and the lower stratosphere, J. Geophys. Res.

859 Atmos., 108(D9), 2003.

860

861 Hauglustaine, D.A. and Brasseur, G.P.: Evolution of tropospheric ozone under anthropogenic

862 activities and associated radiative forcing of climate, J. Geophys. Res. Atmos., 106(D23),

863 pp.32337-32360, 2001.

864

865 Hawas, M.M. and Muneer, T.; Study of diffuse and global radiation characteristics in

866 India. *Energy Conversion and Management*, *24*(2), pp.143-149, 1984.

867

868 Hudson, R.D. and Thompson, A.M.: Tropical tropospheric ozone from total ozone mapping

869 spectrometer by a modified residual method, J. Geophys. Res. Atmos., 103(D17), pp.22129-

870 22145, 1998.

871

872 Hegglin, M. I., Fahey, D. W., McFarland, M., Montzka, S. A., and Nash, E. R.: Twenty questions

873 and answers about the ozone layer: 2014 update, Scientific Assessment of Ozone Depletion: 2014,

874 84 pp., World Meteorological Organization, Geneva, Switzerland, ISBN 978-9966-076-02-1,

875 2015.

876

877   Irion, F.W., Kahn, B.H., Schreier, M.M., Fetzer, E.J., Fishbein, E., Fu, D., Kalmus, P., Wilson,

878   R.C., Wong, S. and Yue, Q.: Single-footprint retrievals of temperature, water vapor and cloud

879   properties from AIRS. Atmospheric Measurement Techniques, 11(2), pp.971-995, 2018.

880

881   Kim, J.H. and Newchurch, M.J.: Climatology and trends of tropospheric ozone over the eastern

882   Pacific Ocean: The influences of biomass burning and tropospheric dynamics, Geophysical

883   research letters, 23(25), pp.3723-3726, 1996.

884

885   Komhyr, W.D., Barnes, R.A., Brothers, G.B., Lathrop, J.A. and Opperman, D.P.: Electrochemical

886   concentration cell ozonesonde performance evaluation during STOIC 1989, J. Geophys. Res.

887   Atmos., 100(D5), pp.9231-9244, 1995.

888

889   Komhyr, W.D.: Nonreactive gas sampling pump. Review of Scientific Instruments, 38(7), pp.981-

890   983, 1967.

891

892   Kumar, R., Naja, M., Satheesh, S.K., Ojha, N., Joshi, H., Sarangi, T., Pant, P., Dumka, U.C.,

893   Hegde, P. and Venkataramani, S.: Influences of the springtime northern Indian biomass burning

894   over the central Himalayas. Journal of Geophysical Research: Atmospheres, 116(D19), 2011.

895

896   Kumar, R., Naja, M., Pfister, G.G., Barth, M.C. and Brasseur, G.P.: Simulations over South Asia

897   using the Weather Research and Forecasting model with Chemistry (WRF-Chem): set-up and

898   meteorological evaluation, Geoscientific Model Development, 5(2), pp.321-343, 2012a.

899

900 Kumar, R., Naja, M., Pfister, G.G., Barth, M.C., Wiedinmyer, C. and Brasseur, G.P.: Simulations

901 over South Asia using the Weather Research and Forecasting model with Chemistry (WRF-

902 Chem): chemistry evaluation and initial results, Geoscientific Model Development, 5(3), pp.619-

903 648, 2012b.

904

905 Lacis, A.A., Wuebbles, D.J. and Logan, J.A.: Radiative forcing of climate by changes in the

906 vertical distribution of ozone, J. Geophys. Res. Atmos., 95(D7), pp.9971-9981, 1990.

907

908 Lal S., S. Venkataramani, S. Srivastava, S. Gupta, M. Naja, T. Sarangi, X. Liu.: Transport effects

909 on the vertical distribution of tropospheric ozone over the tropical marine regions surrounding

910 India, J. Geophys. Res.,118, 1513-1524, doi:10.1002/jgrd.50180, 2013.

911

912 Lal S., S. Venkataramani, N. Chandra, O. R. Cooper, J. Brioude, and M. Naja, Transport effects

913 on the vertical distribution of tropospheric ozone over western India, J. Geophys. Res. Atmos.,

914 119, doi:10.1002/2014JD021854, 2014.

915

916 Lal, S., Venkataramani, S., Naja, M., Kuniyal, J.C., Mandal, T.K., Bhuyan, P.K., Kumari, K.M.,

917 Tripathi, S.N., Sarkar, U., Das, T. and Swamy, Y.V.: Loss of crop yields in India due to surface

918 ozone: An estimation based on a network of observations, Environmental Science and Pollution

919 Research, 24(26), pp.20972-20981, 2017.

920

921 Lawrence, M.G. and Lelieveld, J.: Atmospheric pollutant outflow from southern Asia: a review,

922 Atmospheric Chemistry and Physics, 10(22), pp.11017-11096, 2010.

923

924   Lelieveld, J., Haines, A. and Pozzer, A.: Age-dependent health risk from ambient air pollution: a

925   modelling and data analysis of childhood mortality in middle-income and low-income countries,

926   The lancet Planetary health, 2(7), pp.e292-e300, 2018.

927

928   Livesey, N.J., Logan, J.A., Santee, M.L., Waters, J.W., Doherty, R.M., Read, W.G., Froidevaux,

929   L. and Jiang, J.H.; Interrelated variations of O 3, CO and deep convection in the

930   tropical/subtropical upper troposphere observed by the Aura Microwave Limb Sounder (MLS)

931   during 2004–2011. Atmospheric Chemistry and Physics, 13(2), pp.579-598, 2013.

932

933   Logan, J.A.: Tropospheric ozone: Seasonal behavior, trends, and anthropogenic influence, J.

934   Geophys. Res. Atmos., 90(D6), pp.10463-10482, 1985.

935

936   Lu, X., Zhang, L., Liu, X., Gao, M., Zhao, Y. and Shao, J., 2018. Lower tropospheric ozone over

937   India and its linkage to the South Asian monsoon. *Atmospheric Chemistry and Physics*, *18*(5),

938   pp.3101-3118.

939

940   Maddy, E.S. and Barnet, C.D.: Vertical resolution estimates in version 5 of AIRS operational

941   retrievals, IEEE Transactions on Geoscience and Remote Sensing, 46(8), pp.2375-2384, 2008.

942

943   Mateos, D. and Antón, M.: Worldwide Evaluation of Ozone Radiative Forcing in the UV-B Range

944   between 1979 and 2014. Remote Sensing, 12(3), p.436, 2020.

945

946   McPeters, R.D., Miles, T., Flynn, L.E., Wellemeyer, C.G. and Zawodny, J.M.: Comparison of

947   SBUV and SAGE II ozone profiles: Implications for ozone trends, J. Geophys. Res. Atmos.,

948   99(D10), pp.20513-20524, 1994.

949

950   McPeters, R.D., Labow, G.J. and Johnson, B.J.: A satellite- derived ozone climatology for

951   balloonsonde estimation of total column ozone, J. Geophys. Res. Atmos., 102(D7), pp.8875-8885,

952   1997.

953

954   McPeters, R.D., Labow, G.J. and Logan, J.A.: Ozone climatological profiles for satellite retrieval

955   algorithms, J. Geophys. Res. Atmos., 112(D5), 2007.

956

957   Monahan, K.P., Pan, L.L., McDonald, A.J., Bodeker, G.E., Wei, J., George, S.E., Barnet, C.D. and

958   Maddy, E.: Validation of AIRS v4 ozone profiles in the UTLS using ozonesondes from Lauder,

959   NZ and Boulder, USA, J. Geophys. Res. Atmos., 112(D17), 2007.

960

961   Munro, R., Siddans, R., Reburn, W.J. and Kerridge, B. J.: Direct measurement of tropospheric

962   ozone distributions from space, Nature, 392(6672), pp.168-171, 1998.

963

964   Naja, M., C Mallik, T. Sarangi, V Sheel, S. Lal, SO2 measurements at a high altitude site in the

965   central   Himalayas: Role   of   regional   transport,   Atmospheric   Environment,

966   doi:10.1016/j.atmosenv.2014.08.031, 2014.

967

968 Naja M., Piyush Bhardwaj, N. Singh, Phani Kumar, R. Kumar, N. Ojha, Ram Sagar, S. K.

969 Satheesh, K. Krishna Moorthy and V. R. Kotamarthi: High-frequency vertical profiling of

970 meteorological parameters using AMF1 facility during RAWEX–GVAX at ARIES, Nainital,

971 Current Science, vol 111, issue 1, 2016.

972

973 Nalli, N.R., Barnet, C.D., Reale, A., Tobin, D., Gambacorta, A., Maddy, E.S., Joseph, E., Sun, B.,

974 Borg, L., Mollner, A.K. and Morris, V.R.: Validation of satellite sounder environmental data

975 records: Application to the Cross- track Infrared Microwave Sounder Suite, J. Geophys. Res.

976 Atmos., 118(24), pp.13-628, 2013.

977

978 Nalli, N.R., Gambacorta, A., Liu, Q., Tan, C., Iturbide-Sanchez, F., Barnet, C.D., Joseph, E.,

979 Morris, V.R., Oyola, M. and Smith, J.W.: Validation of Atmospheric Profile Retrievals from the

980 SNPP NOAA-Unique Combined Atmospheric Processing System. Part 2: Ozone, IEEE

981 Transactions on Geoscience and Remote Sensing, 56(1), pp.598-607, 2017.

982

983 Ojha, N., Naja, M., Sarangi, T., Kumar, R., Bhardwaj, P., Lal, S., Venkataramani, S., Sagar, R.,

984 Kumar, A. and Chandola, H.C.: On the processes influencing the vertical distribution of ozone

985 over the central Himalayas: Analysis of yearlong ozonesonde observations, Atmospheric

986 Environment, 88, pp.201-211, 2014.

987

988 Nassar, R., Logan, J.A., Worden, H.M., Megretskaia, I.A., Bowman, K.W., Osterman, G.B.,

989 Thompson, A.M., Tarasick, D.W., Austin, S., Claude, H. and Dubey, M.K. Validation of

990   Tropospheric Emission Spectrometer (TES) nadir ozone profiles using ozonesonde measurements.

991   Journal of Geophysical Research: Atmospheres, 113(D15), 2008.

992

993   Pagano, T.S., Aumann, H.H., Hagan, D.E. and Overoye, K.: Prelaunch and in-flight radiometric

994   calibration of the Atmospheric Infrared Sounder (AIRS), IEEE transactions on geoscience and

995   remote sensing, 41(2), pp.265-273, 2003.

996

997   Pierce, R.B., Al- Saadi, J., Kittaka, C., Schaack, T., Lenzen, A., Bowman, K., Szykman, J., Soja,

998   A., Ryerson, T., Thompson, A.M. and Bhartia, P.: Impacts of background ozone production on

999   Houston and Dallas, Texas, air quality during the Second Texas Air Quality Study field mission,

1000 J. Geophys. Res. Atmos., 114(D7), 2009.

1001

1002 Pittman, J.V., Pan, L.L., Wei, J.C., Irion, F.W., Liu, X., Maddy, E.S., Barnet, C.D., Chance, K.

1003 and Gao, R.S.: Evaluation of AIRS, IASI, and OMI ozone profile retrievals in the extratropical

1004 tropopause region using in situ aircraft measurements, J. Geophys. Res. Atmos., 114(D24), 2009.

1005

1006 Ramaswamy, V., Boucher, O., Haigh, J., Hauglustaine, D., Haywood, J., Myhre, G., Nakajima,

1007 T., Shi, G.Y. and Solomon, S.: Radiative forcing of climate change. Climate change 2001: the

1008 scientific basis. Contribution of working group I to the third assessment report of the

1009 intergovernmental panel on climate change. *DJ Griggs, M Noguer, PJ van der Linden, X Dai, K*

1010 *Maskell and CA Johnson (Cambridge: Cambridge University Press) pp*, *350*, p.416, 2001.

1011

1012   Rawat, P., Naja, M., Thapliyal, P.K., Srivastava, S., Bhardwaj, P., Kumar, R., Bhatacharjee, S.,

1013   Venkatramani, S., Tiwari, S.N. and Lal, S.: Assessment of vertical ozone profiles from INSAT-

1014   3D sounder over the Central Himalaya. Current Science, 119(7), p.1113, 2020.

1015   Rawat, P. and Naja, M.: Remote sensing study of ozone, NO2, and CO: some contrary effects of

1016   SARS-CoV-2 lockdown over India. Environ Sci Pollut Res, https://doi.org/10.1007/s11356-021-

1017   17441-2, 2021.

1018   Rodgers, C.D., 1976. Retrieval of atmospheric temperature and composition from remote

1019   measurements of thermal radiation. *Reviews of Geophysics*, *14*(4), pp.609-624.

1020

1021   Rodgers, C.D., 1990. Characterization and error analysis of profiles retrieved from remote

1022   sounding measurements. *Journal of Geophysical Research: Atmospheres*, *95*(D5), pp.5587-5595.

1023

1024   Rodgers, C.D. and Connor, B.J., 2003. Intercomparison of remote sounding instruments. *Journal*

1025   *of Geophysical Research: Atmospheres*, *108*(D3).

1026

1027   Sarangi T., M. Naja, N. Ojha, R. Kumar, S. Lal, S. Venkataramani, A. Kumar, R. Sagar and H. C.

1028   Chandola: First simultaneous measurements of ozone, CO and NO_y at a high altitude regional

1029   representative site in the central Himalayas, J. Geophys. Res., 119, doi:10.1002/2013JD020631,

1030   2014.

1031

1032   Schwartz, M., Froidevaux, L., Livesey, N. and Read, W.: MLS/Aura Level 2 Ozone (O3) Mixing

1033   Ratio V004, Greenbelt, MD, USA, Goddard Earth Sciences Data and Information Services Center

1034   (GES DISC), 10.5067/Aura/MLS/DATA2017, 2015.

1035

1036   Shindell, D., Kuylenstierna, J.C., Vignati, E., van Dingenen, R., Amann, M., Klimont, Z.,

1037   Anenberg, S.C., Muller, N., Janssens-Maenhout, G., Raes, F. and Schwartz, J.: Simultaneously

1038   mitigating near-term climate change and improving human health and food security, Science,

1039   335(6065), pp.183-189, 2012.

1040

1041   Smit, H.G., Straeter, W., Johnson, B.J., Oltmans, S.J., Davies, J., Tarasick, D.W., Hoegger, B.,

1042   Stubi, R., Schmidlin, F.J., Northam, T. and Thompson, A.M.: Assessment of the performance of

1043   ECC- ozonesondes under quasi- flight conditions in the environmental simulation chamber:

1044   Insights from the Juelich Ozone Sonde Intercomparison Experiment (JOSIE), Journal of

1045   Geophysical Research: Atmospheres, 112(D19), 2007.

1046

1047   Srivastava S., Manish Naja, V. Thouret: Influences of regional pollution and long range transport

1048   over Hyderabad using ozone data from MOZAIC, Atmospheric Environment, *117*, pp.135-146,

1049   2015.

1050

1051   Stevenson, D.S., Young, P.J., Naik, V., Lamarque, J.F., Shindell, D.T., Voulgarakis, A., Skeie,

1052   R.B., Dalsoren, S.B., Myhre, G., Berntsen, T.K. and Folberth, G.A.: Tropospheric ozone changes,

1053   radiative forcing and attribution to emissions in the Atmospheric Chemistry and Climate Model

1054   Intercomparison Project (ACCMIP), Atmos. Chem. Phys., 13(6), pp.3063-3085, 2013.

1055

1056   Susskind, J., Barnet, C.D. and Blaisdell, J.M.: Retrieval of atmospheric and surface parameters

1057   from AIRS/AMSU/HSB data in the presence of clouds, IEEE Transactions on Geoscience and

1058   Remote Sensing, 41(2), pp.390-409, 2003.

1059

1060   Susskind, J., Barnet, C., Blaisdell, J., Iredell, L., Keita, F., Kouvaris, L., Molnar, G. and Chahine,

1061   M.: Accuracy of geophysical parameters derived from Atmospheric Infrared Sounder/Advanced

1062   Microwave Sounding Unit as a function of fractional cloud cover, J. Geophys. Res. Atmos.,

1063   111(D9), 2006.

1064

1065   Veefkind, J.P., de Haan, J.F., Brinksma, E.J., Kroon, M. and Levelt, P.F.: Total ozone from the

1066   Ozone Monitoring Instrument (OMI) using the DOAS technique, IEEE transactions on geoscience

1067   and remote sensing, 44(5), pp.1239-1244, 2006.

1068

1069   Verstraeten, W. W., Boersma, K. F., Zörner, J., Allaart, M. A. F., Bowman, K. W., and Worden,

1070   J. R.: Validation of six years of TES tropospheric ozone retrievals with ozonesonde measurements:

1071   implications for spatial patterns and temporal stability in the bias, Atmos. Meas. Tech., 6, 1413–

1072   1423, https://doi.org/10.5194/amt-6-1413-2013, 2013.

1073

1074   Wang, W.C., Zhuang, Y.C. and Bojkov, R.D.: Climate implications of observed changes in ozone

1075   vertical distributions at middle and high latitudes of the Northern Hemisphere, Geophysical

1076   research letters, 20(15), pp.1567-1570, 1993.

1077

1078 Wang, B., R. Wu, K.-M. Lau: Interannual variability of Asian summer monsoon: Contrast between

1079 the Indian and western North Pacific-East Asian monsoons. J. Climate, 14, 4073-4090, 2001.

1080

1081 Wang, H.R., Damadeo, R., Flittner, D., Kramarova, N., Taha, G., Davis, S., Thompson, A.M.,

1082 Strahan, S., Wang, Y., Froidevaux, L. and Degenstein, D.: Validation of SAGE III/ISS Solar

1083 Occultation Ozone Products With Correlative Satellite and Ground- Based Measurements. Journal

1084 of Geophysical Research: Atmospheres, 125(11), p.e2020JD032430, 2020.

1085 Wang, W., Cheng, T., van der A, R.J., de Laat, J. and Williams, J.E.: Verification of the

1086 Atmospheric Infrared Sounder (AIRS) and the Microwave Limb Sounder (MLS) ozone algorithms

1087 based on retrieved daytime and night-time ozone, Atmos. Meas. Tech., 14(2), pp.1673-1687, 2021.

1088

1089 Zhang, L., Jacob, D.J., Liu, X., Logan, J.A., Chance, K., Eldering, A. and Bojkov, B.R.:

1090 Intercomparison methods for satellite measurements of atmospheric composition: application to

1091 tropospheric ozone from TES and OMI. Atmospheric Chemistry and Physics, 10(10), pp.4725-

1092 4739, 2010.

1093 Zhu, T., W. Lin,Y. Song, X. Cai, H. Zou, L. Kang, L. Zhou, and H. Akimoto: Downward transport

1094 of ozone-rich air near Mt. Everest, Geophys. Res. Lett., 33, L23809,doi:10.1029/2006GL027726,

1095 2006.

1096

1097 Ziemke, J.R., Chandra, S. and Bhartia, P. K.: Two new methods for deriving tropospheric column

1098 ozone from TOMS measurements: Assimilated UARS MLS/HALOE and convective- cloud

1099 differential techniques, J. Geophys. Res. Atmos., 103(D17), pp.22115-22127, 1998.

1100

1101   Ziemke, J.R., Chandra, S., Duncan, B.N., Froidevaux, L., Bhartia, P.K., Levelt, P.F. and Waters,

1102   J.W.: Tropospheric ozone determined from Aura OMI and MLS: Evaluation of measurements and

1103   comparison with the Global Modeling Initiative's Chemical Transport Model, J. Geophys. Res.

1104   Atmos., 111(D19), 2006.

1105

1106

1107

1108

1109

1110

1111

1112

1113

1114

1115

1116

1117

1118

1119

1120

1121

1122

1123 **Table 1.** The mean values and corresponding standard errors of ozone mixing ratio (ppbv) from

1124 ozonesonde, ozonesonde(AK) and AIRS over Nainital at six pressure levels and during winter,

1125 spring, summer-monsoon, autumn are given. The number of ozonesonde flights during four

1126 seasons are mentioned in the bracket.

Pressure levels		706 (hPa)	496 (hPa)	300 (hPa)	103 (hPa)	29 (hPa)	14.4 (hPa)
Winter (61)	ozonesonde	55.1±0.9	54.4±0.7	69.5±2.8	238.8±15.0	4569.3±67.8	7620.6±140.1
	ozonesonde (AK)	48.6±0.4	55.9±0.6	70.4±1.8	187.3±3.6	5249.1±78.8	8214.9±105.7
	AIRS	46.5±0.3	52.2±0.6	68.7±1.2	354.4±8.4	4428.2±55.8	6616.4±56.0
Spring (72)	ozonesonde	71.6±1.8	70.2±1.5	81.5±2.8	223.9±12.7	4747.0±42.6	8242.3±101.6
	ozonesonde (AK)	58.7±0.7	69.1±1.1	80.3±1.4	221.8±3.6	5137.8±63.4	8784.4±96.6
	AIRS	55.3±0.4	60.7±0.7	78.6±1.0	389.2±6.0	4687.4±38.2	7852.4±97.0
Summer-monsoon (55)	ozonesonde	53.0±2.7	65.1±2.7	82.1±2.5	138.6±3.4	4642.9±26.4	8493.6±91.1
	ozonesonde (AK)	44.1±1.2	62.3±1.7	68.7±1.7	224.3±3.4	5271.3±44.6	9233.8±72.4
	AIRS	48.8±0.5	57.5±0.5	63.6±0.6	267.4±5.5	4710.0±48.2	8333.1±82.5
Autumn (54)	ozonesonde	53.0±1.1	63.8±1.6	72.7±1.6	144.6±6.2	4439.3±28.2	8613.7±77.5
	ozonesonde (AK)	50.4±0.5	61.0±0.8	64.1±0.9	169.0±2.0	5086.3±38.7	9035.8±80.7
	AIRS	46.0±0.3	51.3±0.4	56.9±30.5	241.8±3.6	4635.4±43.9	7984.9±97.6

1127 **Table 2.** Coefficient of determination (r^2) of three IR satellite sensors (AIRS, IASI and CrIS) ozone

1128 retrieval in five broad layers with respect to ozonesonde observations.

	Coefficient of determination (r^2)		
	AIRS	IASI	CrIS
600 - 800 hPa	0.52	0.34	0.09
300 - 600 hPa	0.44	0.31	0.22
100 - 300 hPa	0.45	0.44	0.45
50-100 hPa	0.87	0.76	0.82
10 - 50 hPa	0.94	0.80	0.94

1129

1130

1131 **Table 3.** Total column ozone (TCO) differences in DU between AIRS, OMI and ozonesonde,

1132 during twelve months.

TCO Diff. (DU)	Jan	Feb	Mar	Apr	May	Jun	Jul	Aug	Sep	Oct	Nov	Dec
AIRS-OMI	-3.9	2.2	-1.8	13.2	16.7	18	-2.2	17.2	22.1	13.2	0.0	-2.7
AIRS-ozonesonde	-2.1	3.5	6.0	8.1	19.4	11.8	-2.3	22.3	21.6	15.0	5.6	5.2

1133

1134

1135

1136

1137

1138
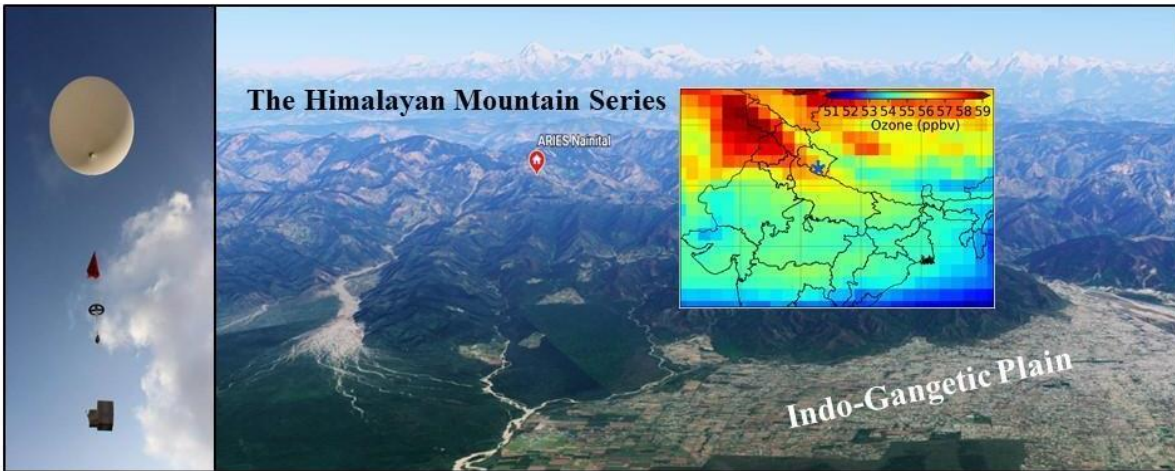
1139

Figure 1. Location (red color circle) of the balloon launching site (Map from Google Earth, 2021) situated in the Aryabhatta Research Institute of Observational Sciences (ARIES) (29.4º N, 79.5º E, and 1793 m elevation), Nainital in the central Himalaya. The spatial distribution of ozone (AIRS) at 500 hPa is also shown over northern India and the location of the site is marked with a blue star. A photo of balloon, together with parachute, unwinder, ozonesonde along with GPS-radiosonde above the observation site is also shown at the left.

1146

1147

1148

1149

1150
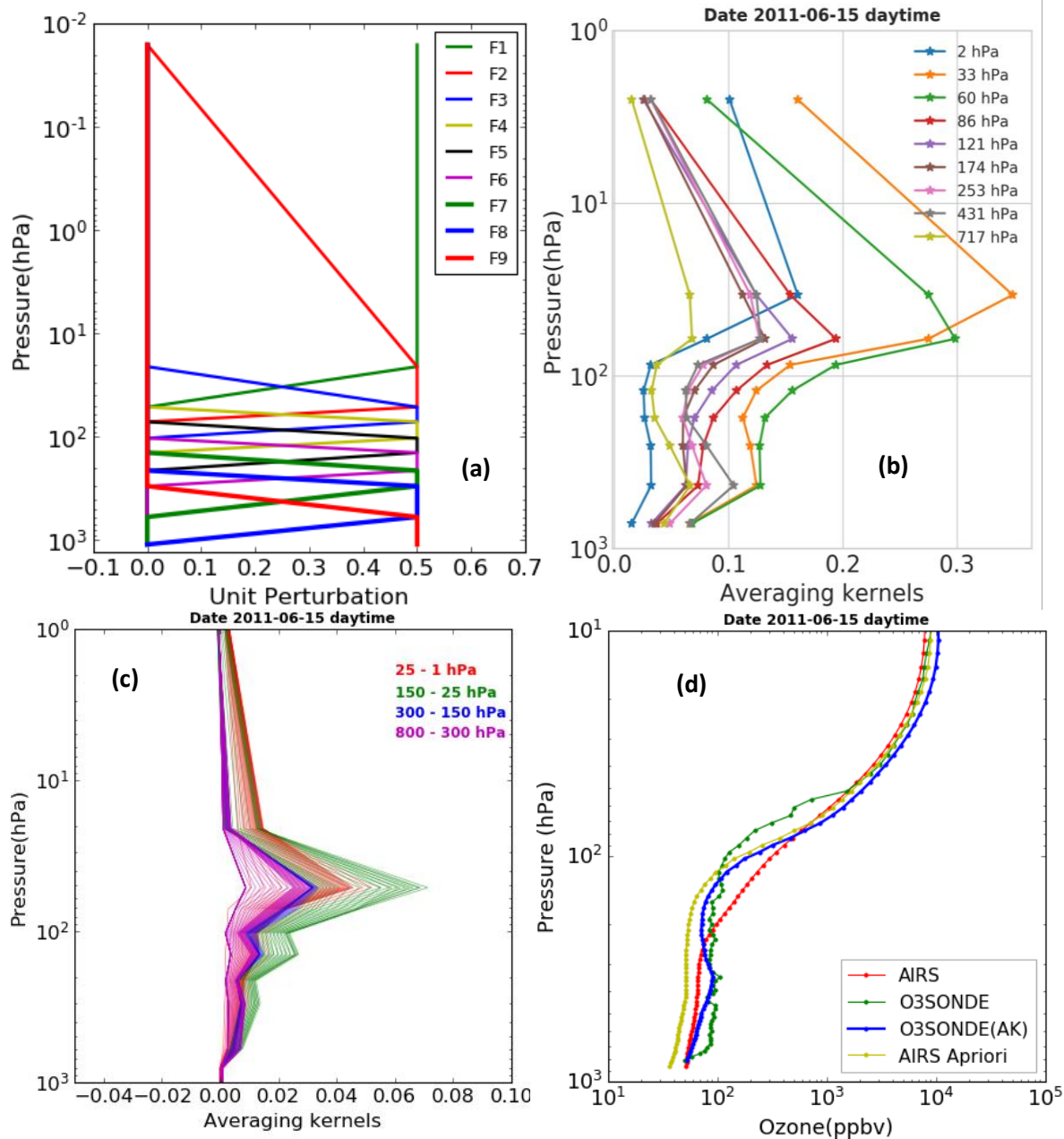
Figure 2. (a) Nine trapezoid functions used for ozone retrieval in AIRS-V6. (b) AIRS ozone averaging kernel matrix over Nainital at 9 levels vertical grid. (c) Calculated AIRS averaging kernel matrices at 100 RTA grids after applying the trapezoid function. (d) An example of ozone profiles using different data sets for 15 Jun 2011 over the observation site.
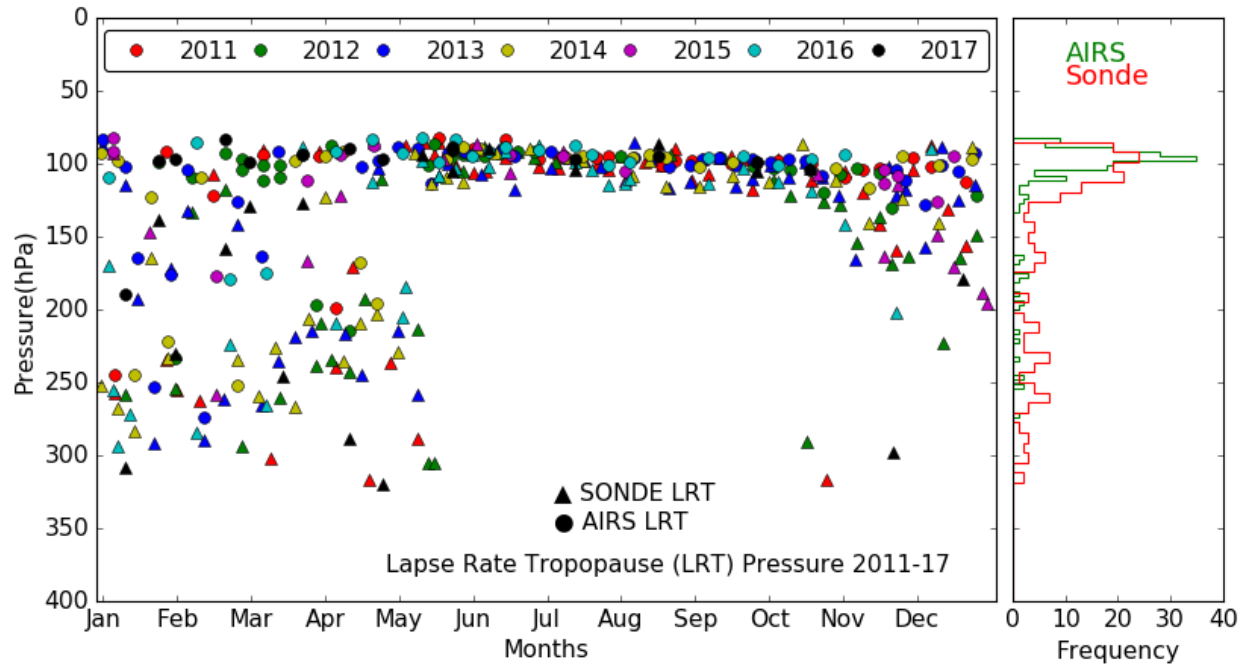
Figure 3. Lapse rate tropopause pressure monthly variation from balloon-borne and AIRS observations and respective frequency distributions during 2011 - 2017.

1171

Ozonesonde   AIRS
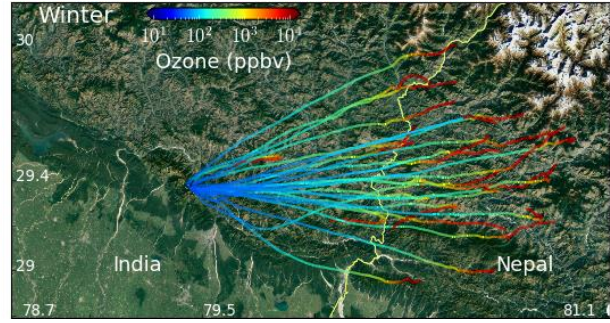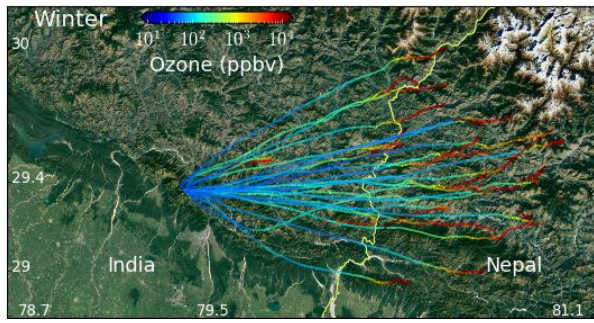
1172
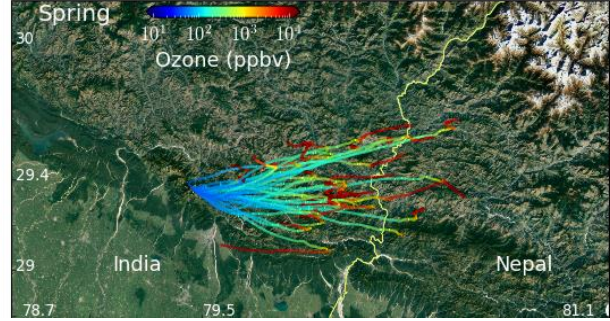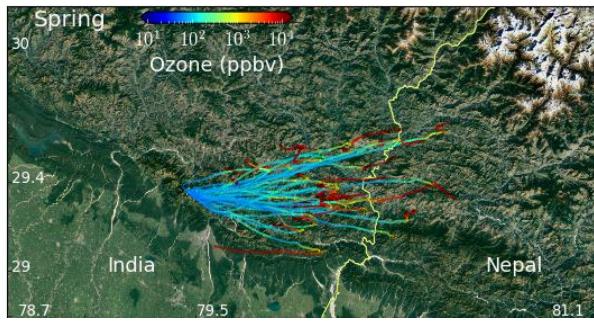
1173
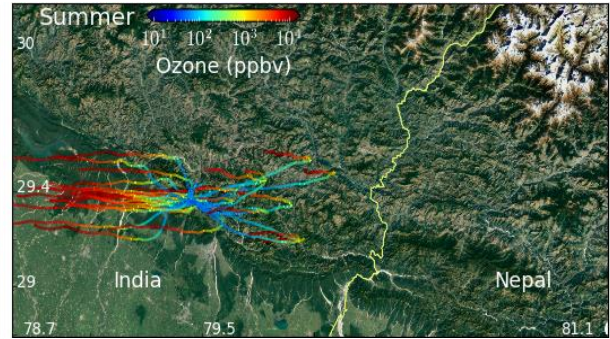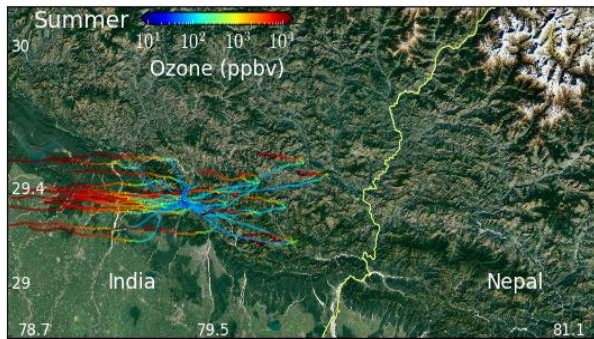
1174
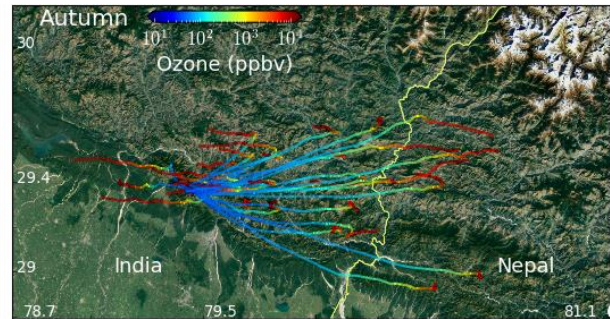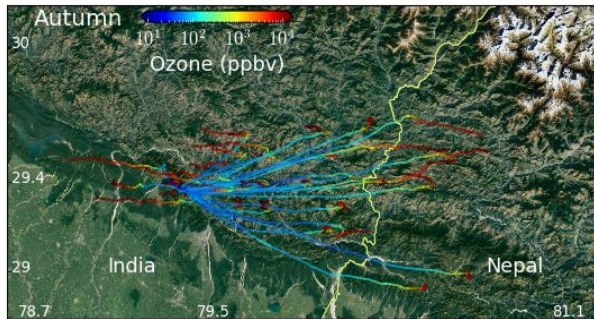
1175
1176
1177

Figure 4. Spatial distribution of ozone using all ozone soundings (left) launched from ARIES, Nainital, India (Map from Google Earth, 2021) along with the balloon trajectories. Ozone spatial distribution from AIRS (right), following the balloon tracks, is also shown. It could be seen that the balloon reaches Nepal many times in the winter and autumn seasons.

1182
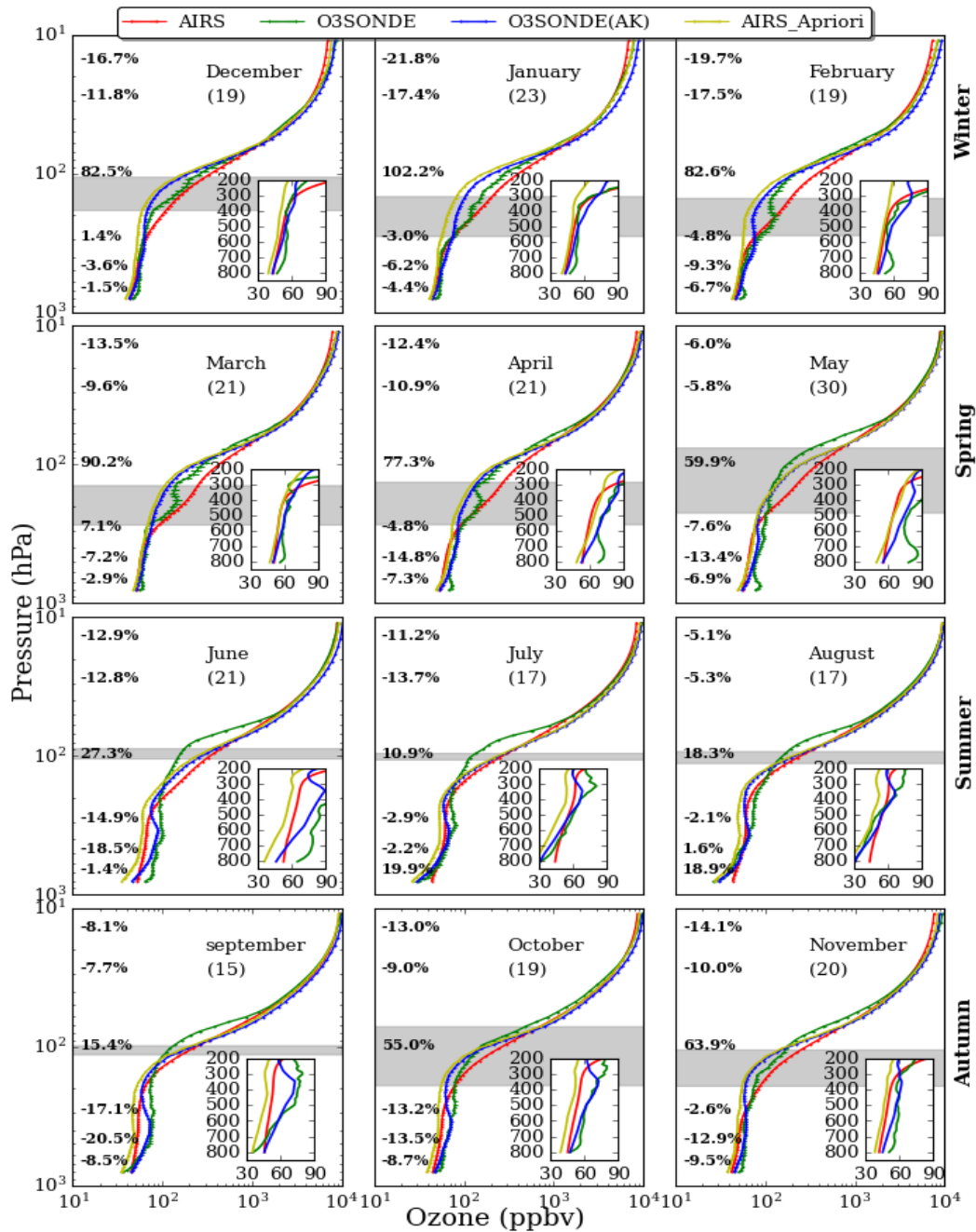
Figure 5. Monthly averaged (2011-2017) ozone profiles of ozonesonde, AIRS, ozonesonde(AK) and AIRS a-priori over Nainital in the central Himalaya. The percentage difference [(AIRS − ozonesonde(AK))/ozonesonde(AK)]*100 at 706, 496, 300, 103, 29, and 14.4 hPa are also written at respective altitudes. The standard error corresponding to each profile is also shown with errorbars. The number of ozonesonde for different months is written in the bracket and grey shaded area shows the tropopause (mean±sigma) from balloon-borne observations.

1190
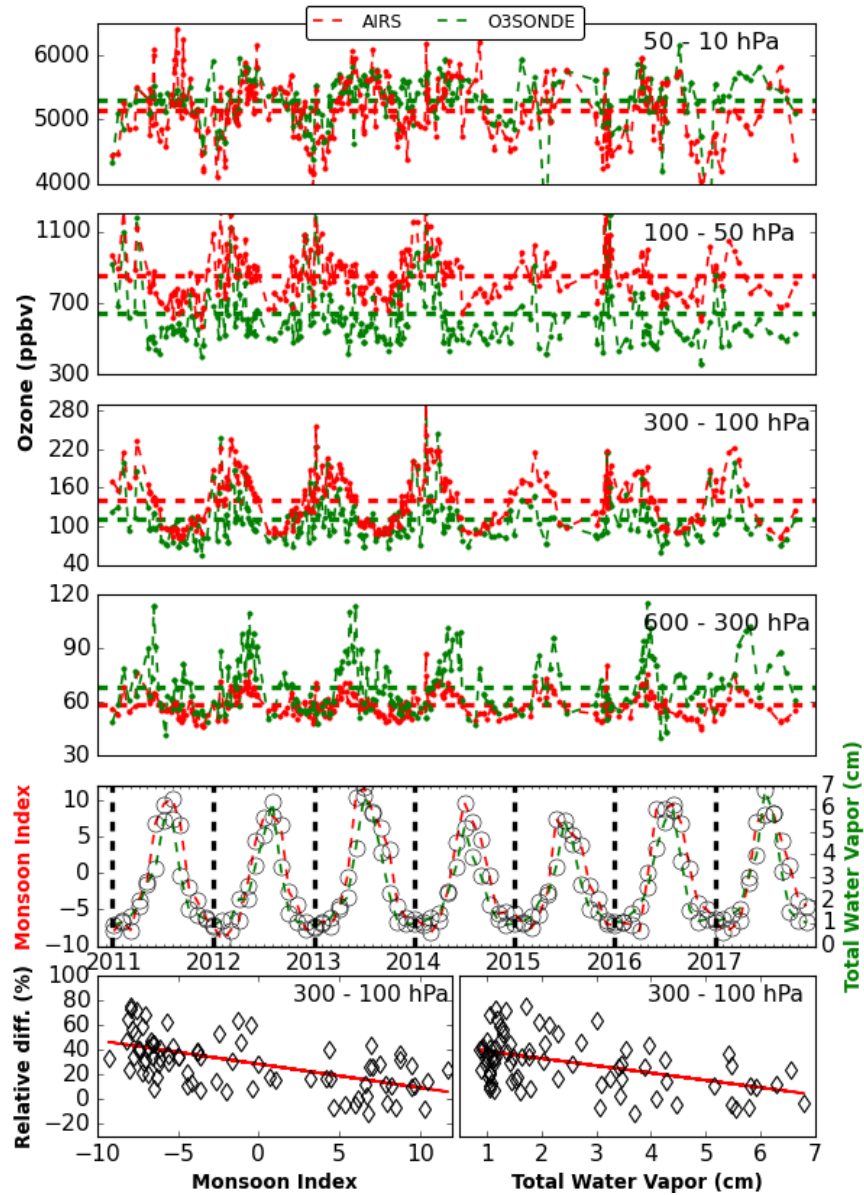
1191

1192

1193 **Figure 6.** Average variations in ozone mixing ratios at four defined layers, characterizing the

1194 middle stratosphere (50 - 10 hPa), the lower stratosphere (100 - 50 hPa), the upper troposphere

1195 (300 - 100 hPa), and the middle troposphere (600 - 300 hPa), respectively. The red and green dash

1196 horizontal lines show the average ozone mixing ratios in the defined layers from AIRS and

1197 ozonesonde, respectively for 2011 to 2017. The monthly variation of the total column water vapor

1198 (cm) along with the monsoon index is also shown. The scattered plot of ozone relative difference

1199 (%) [(AIRS-O3SONDE)/O3SONDE]*100, with monsoon index and total water vapor in the upper

1200 troposphere (300 - 100 hPa) is also shown at the bottom.
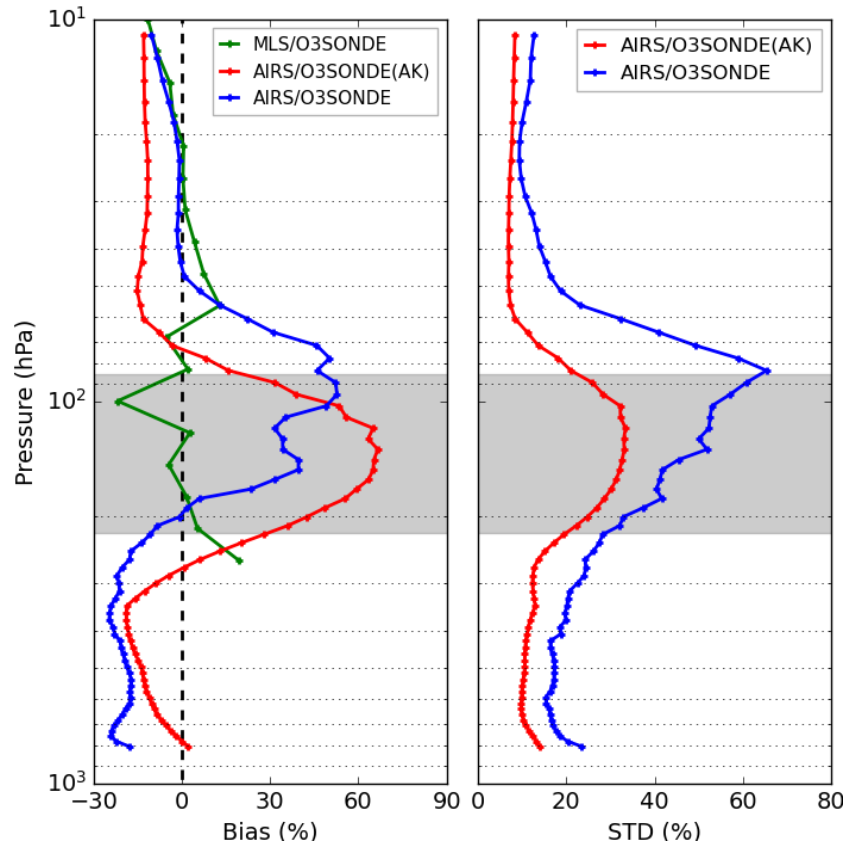
Figure 7. Statistical error analysis (Bias and standard deviation) of AIRS retrieved ozone with ozonesonde and ozonesonde (AK) for collocated data of seven years (2011 - 2017). The Bias between collocated data of MLS (261 hPa - 10 hPa) and ozonesonde over Nainital during 2011 - 2017 is also shown with green profile. The grey shaded area shows the tropopause region from balloon-borne radiosondes observations.
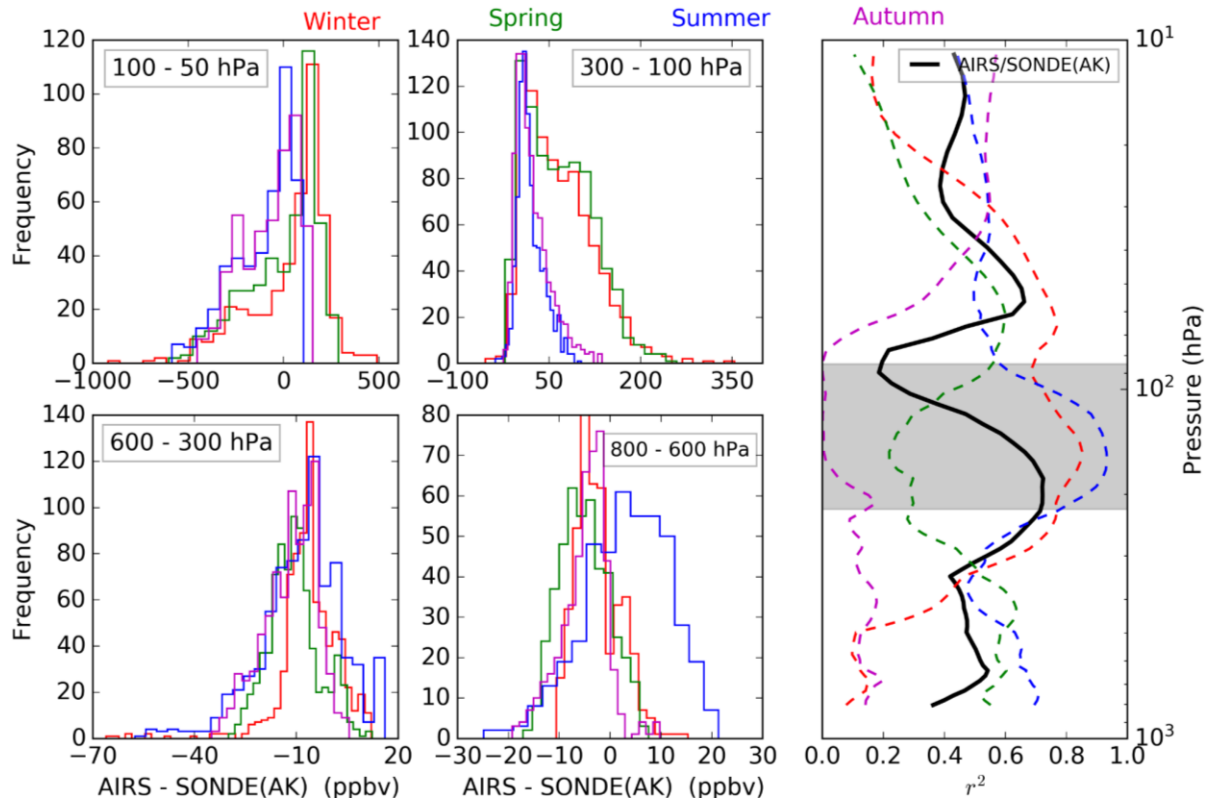
Figure 8. Histogram difference between AIRS ozone and ozonesonde(AK) in the four defined layers. The average correlation profiles between AIRS ozone and ozonesonde(AK) are shown on the right during winter (red), spring (green), summer-monsoon (blue), and autumn (magenta). The black line is for the entire data set. The grey shaded area shows the tropopause region from balloon-borne radiosondes observations.
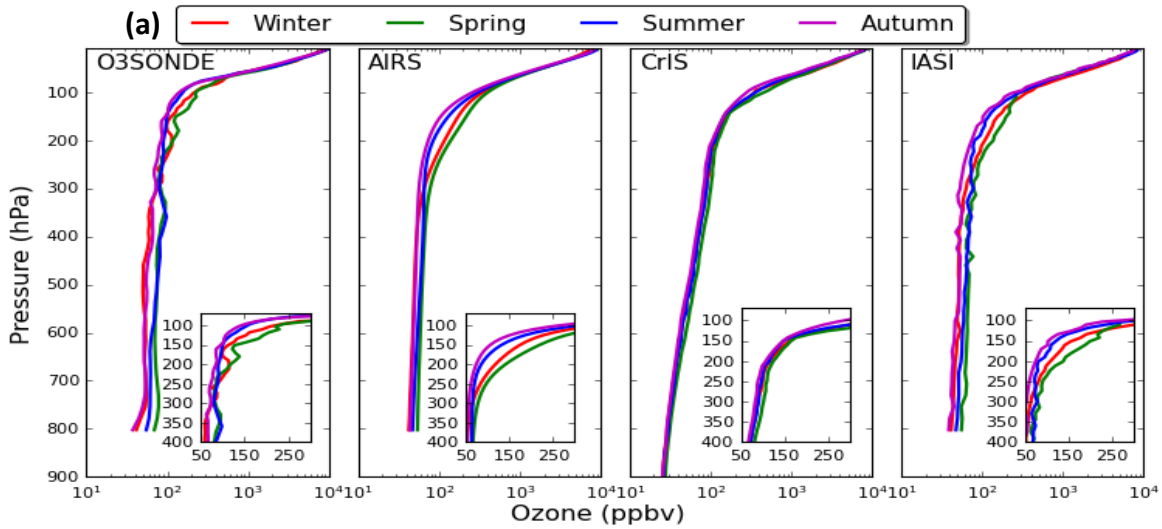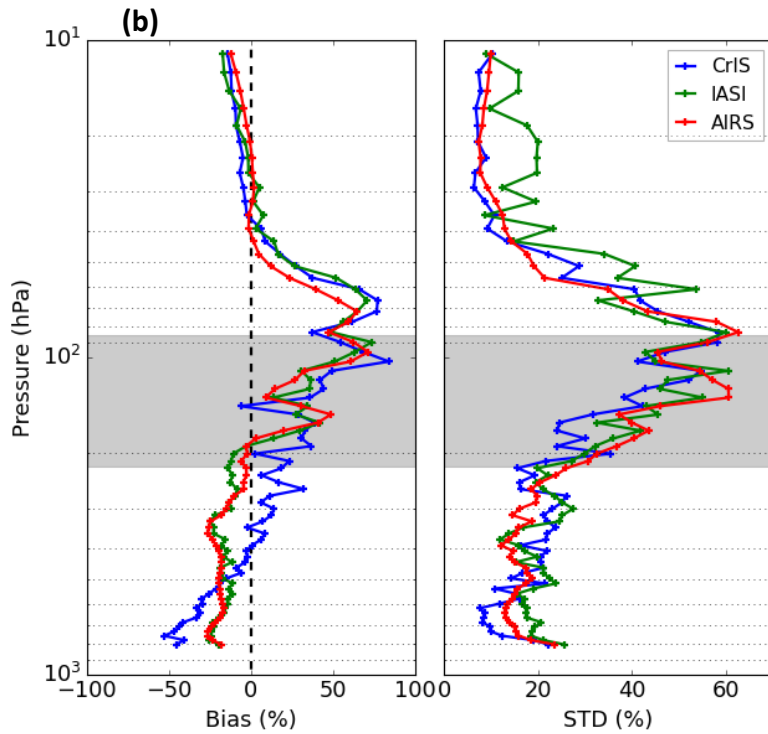
Figure 9. **(a)** Seasonal ozone profiles of three IR satellites (IASI, AIRS, and CrIS) for a smaller sample size (April 2014 to April 2015). The IASI and CrIS products are generated using the AIRS heritage algorithm (NOAA) and only zero quality flags (QC=0) of retrieval are used. **(b)** Statistical error analysis for the three IR satellites retrieved ozone without applying the averaging kernel information. The grey shaded area shows the tropopause region from balloon-borne observations.
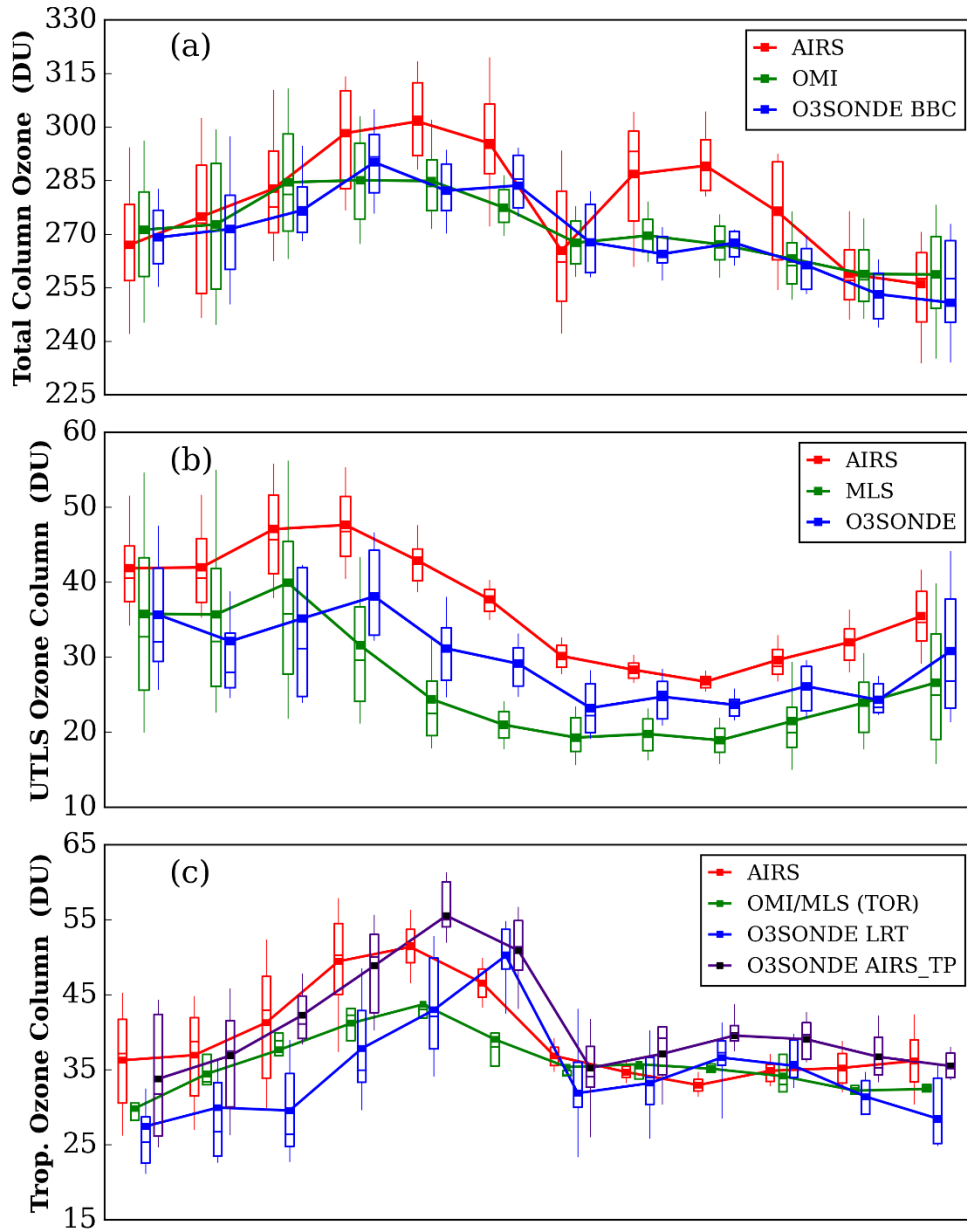
Figure 10. (a) Monthly average variations of total column ozone (TCO) for AIRS, OMI, and ozonesonde (Balloon Burst Climatology) over the central Himalaya for the 2011-2017 period. (b) Monthly average variation of UTLS ozone column for AIRS, MLS, and ozonesonde, over the central Himalayas for the 2011-2017 period. (c) Monthly average variations of tropospheric ozone column of AIRS, OMI/MLS (Tropospheric Ozone Residual), and ozonesonde (LRT – sonde lapse rate), over the central Himalayas for the 2011-2017 period. The ozonesonde tropospheric ozone column is also shown using AIRS tropopause (AIRS_TP). In the box plot, lower and upper edges of the boxes represent the 25th and 75th percentiles. The whiskers below and above are 10th and 90th percentiles.
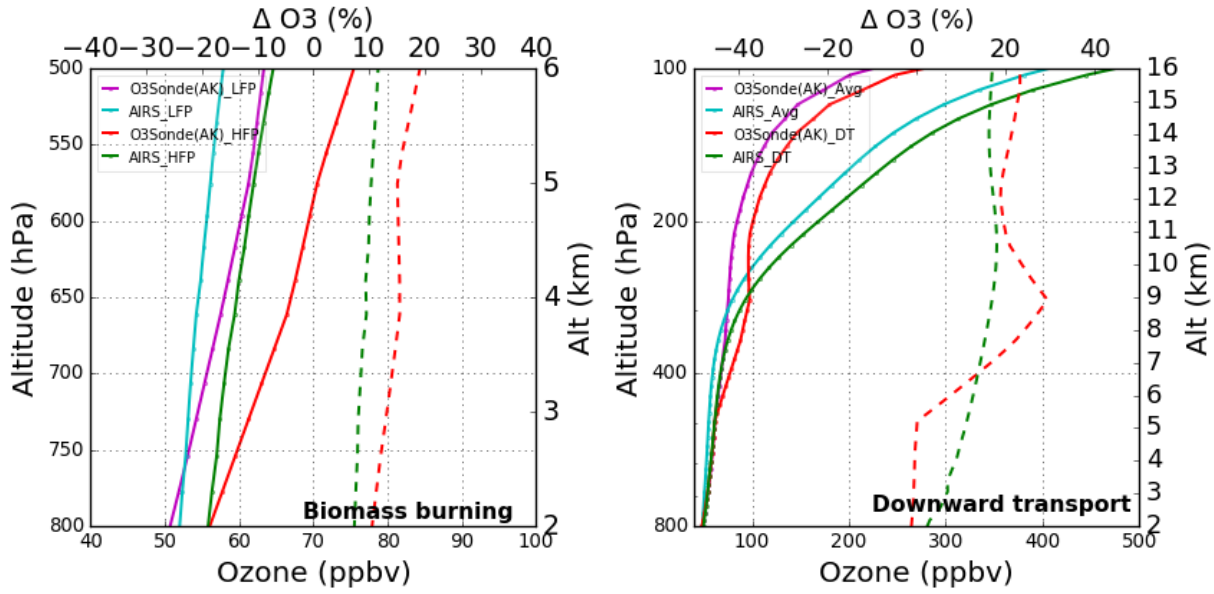
1236

1237   **Figure 11. (a)** Vertical ozone profiles of AIRS ozone and ozonesonde(AK) during low fire period

1238   (LFP) and high fire period (HEP). The solid lines correspond to ozone profiles while the dotted

1239   lines show percentage increase in ozonesonde (red) and AIRS (green) profiles during biomass
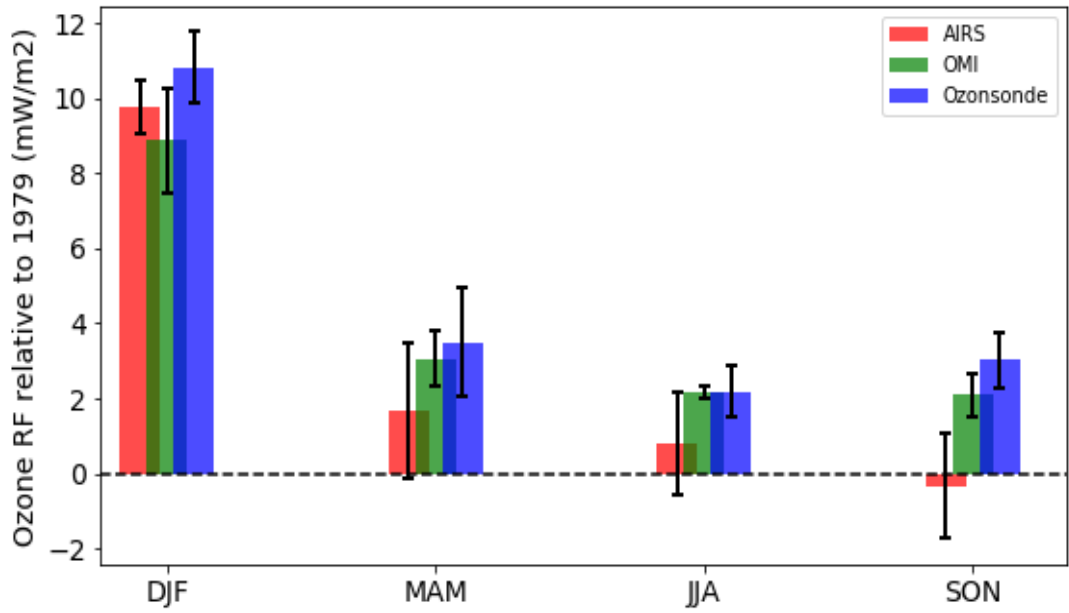
1240   burning events. **(b)** Vertical ozone profiles of AIRS ozone and ozonesonde(AK) during events of

1241   downward transport. Dotted line shows ozone enhancement during downward transport events.

1242

1243

1244

Figure 12. Seasonal average ozone UV radiative forcing (RF) relative to 1979 as calculated from ozonesonde, OMI, and AIRS total ozone data for the 2011 - 2017 period. Spreads correspond to one standard deviation.